AGU PUBLICATIONS

JGR

Journal of Geophysical Research: Oceans

RESEARCH ARTICLE

10.1002/2014JC009857

Key Points:
- ROMS simulation of the Arabian Sea at 6 km of resolution
- Characterization of the Great Whirl life cycle
- Assessment of the Rossby waves influence on the Great Whirl life cycle

Correspondence to:
C. Vic,
clement.vic@univ-brest.fr

Citation:
Vic, C., G. Roullet, X. Carton, and X. Capet (2014), Mesoscale dynamics in the Arabian Sea and a focus on the Great Whirl life cycle: A numerical investigation using ROMS, *J. Geophys. Res. Oceans*, *119*, 6422–6443, doi:10.1002/2014JC009857.

Received 27 JAN 2014
Accepted 3 SEP 2014
Accepted article online 9 SEP 2014
Published online 22 SEP 2014

Mesoscale dynamics in the Arabian Sea and a focus on the Great Whirl life cycle: A numerical investigation using ROMS

C. Vic[1], G. Roullet[1], X. Carton[1], and X. Capet[2]

[1]Laboratoire de Physique des Océans, UMR 6523, CNRS/Ifremer/IRD/UBO, Brest, France, [2]IPSL/LOCEAN, UMR 7159, CNRS/UPMC/IRD/MNHN, 4 Place Jussieu, Paris, France

Abstract The Great Whirl (GW) is a persistent anticyclonic mesoscale eddy that is observed seasonally in the Arabian Sea during a period embedding the 3 months of the southwest monsoon (June–July–August) at a quasi-steady location. Its dynamics remain unclear despite it being one of the largest coherent vortices in the world ocean. Realistic regional numerical experiments using ROMS are performed to investigate the life cycle of the GW, which is not well resolved by sparse available in situ measurements in the region. Using a set of sensitivity experiments and an accurate temporal characterization of the eddy properties (including position, radius, depth, and vorticity) we (i) confirm the role of basin-scale downwelling Rossby waves in the GW generation, (ii) clarify the role of the monsoonal strong anticyclonic wind in its maintenance and barotropization, and (iii) suggest a connection between basin-scale Rossby wave dynamics and GW collapse.

1. Introduction

The circulation in the Arabian Sea is highly seasonal due to the reversing winds in the region, blowing mainly from the southwest in summer (southwest monsoon, SWM, commonly occurring from June to August) and from the northeast in winter (northeast monsoon, NEM, from December to February) [*Bruce*, 1983]. The basin circulation mainly follows the large-scale wind stress curl pattern, being cyclonic during the NEM and anticyclonic during the SWM [*Shetye et al*., 1994]. Circulations during the spring and fall intermonsoons (SIM, from March to May and FIM, from September to November, respectively) are often interpreted as relaxation of wind forced circulations during the monsoons [*Lee et al*., 2000].

The western boundary current along the Eastern African Coast, between the equator and 4−9°N (depending on the season), known as the Somali Current (SC), also reverses [*Schott*, 1983]. This seasonal shift of the currents is a distinguishing feature of the Arabian Sea due to the wind seasonality (the word *monsoon* comes from the Portuguese *monção*, itself from the Arabic *mawsim* which means *season*). To first order, it can be explained by the low latitude of the region, which implies a rapid adjustment of the dynamics by planetary waves [*Lighthill*, 1969]. It has however recently been shown that retroaction at interannual time scales exist [*Beal et al*., 2013]. During the SWM, the SC flows northward and is accompanied by a coastal upwelling triggered by the winds parallel to the coast (Figure 1).

At the northern end of the SC, during the SWM, a remarkable mesoscale anticyclonic eddy has been observed with in situ [*Leetmaa et al*., 1982; *Schott and Quadfasel*, 1982; *Wirth et al*., 2002] and satellite [*Schott*, 1983; *Beal and Donohue*, 2013] data. The position of the so-called Great Whirl (as first described by sailors), located close to the Somali coast between 5°N and 10°N and embedded in the very turbulent environment of the western boundary upwelling (winds blow parallel to the coast in a direction triggering upwelling), is quasi-steady from the onset of the monsoon until the end of October, about 1 month after the end of the SWM. Being the dominant persistent mesoscale structure of the region, it has been studied for decades.

The onset of the GW, its life cycle, and the mechanisms underlying its collapse are issues which have received attention, but which are not yet totally resolved. In particular, the respective role of local forcing by the wind versus remote effects induced by Rossby waves remains to be settled. *Schott and Quadfasel* [1982] observed in situ westward propagating signals after the onset of the SWM, which they interpreted as a possible first-mode Rossby wave that reflects at the coast into shorter modes and leads to the formation of

© 2014. American Geophysical Union. All Rights Reserved.

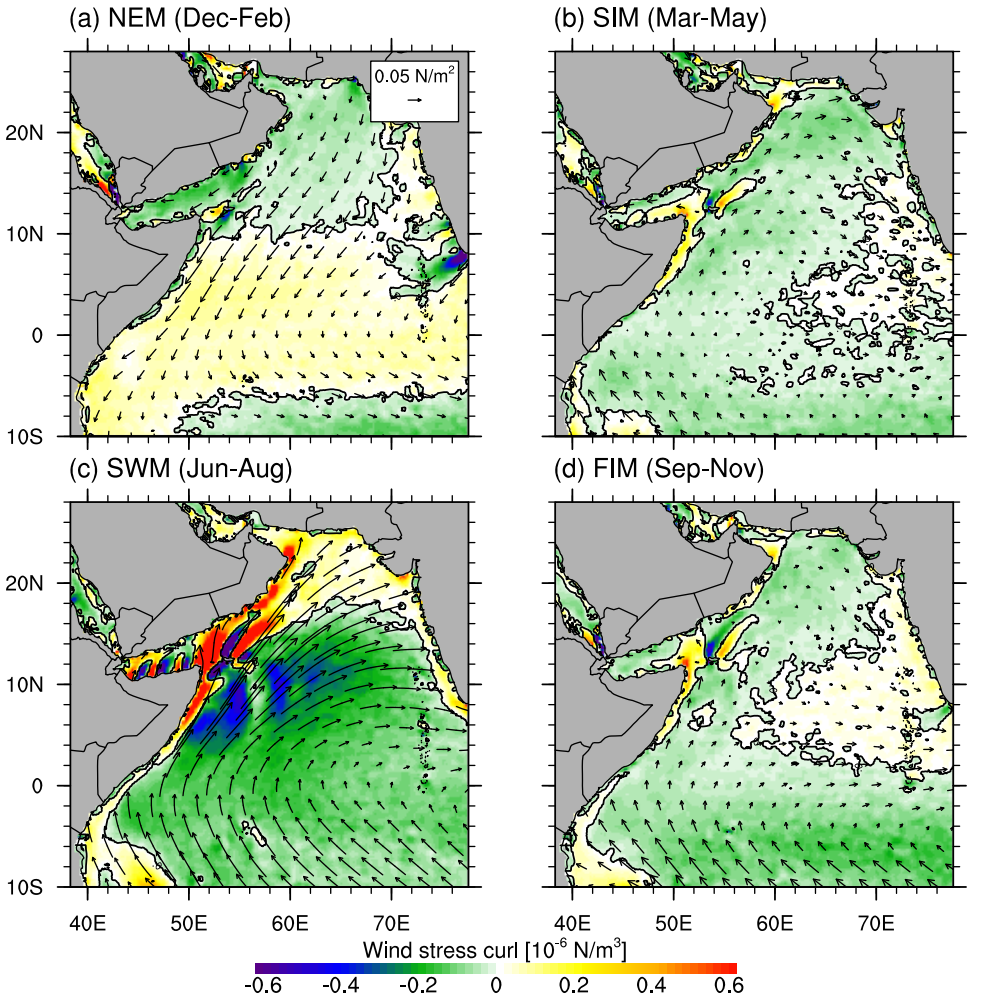

Figure 1. Wind stress (arrows) and wind stress curl (contours) derived from QuikSCAT climatology (see Table 1 for details) and averaged for the periods (a) NEM (December–February), (b) SIM (March–May), (c) SWM (June–August), and (d) FIM (September–November). Black contour is the zero wind stress curl.

eddies at the boundary. A numerical study of *McCreary et al*. [1993] highlighted the arrival of annual Rossby waves from the tip of India which could be a remote forcing of many structures at the western boundary of the basin. This has recently been confirmed by the analysis of 18 years of satellite data that shows positive sea surface height anomalies reaching the coast and then swirling into what becomes the GW [*Beal and Donohue*, 2013]. In a more general framework, the importance of wave-like signals emerging from the eastern side of the basin in the dynamics of the Arabian Sea has also been highlighted by *Kim et al*. [2001] and *Rao et al*. [2010] and is consistent with the low-latitude planetary wave dynamics, e.g., in terms of high propagation speed [*Lighthill*, 1969].

On the other hand, the wind has often been considered as the dominant forcing of the GW because the eddy is located where the wind stress curl is the most negative, hence anticyclonic favorable [*Schott*, 1983; *Luther and O'Brien*, 1989]. The review of *Schott and McCreary* [2001] concluded that local forcing dominates the generation and variability of the GW. The Findlater Jet is defined as the monsoonal southwesterly wind maximum in the Arabian Sea [*Findlater*, 1969]. It is characterized by a zero wind stress curl along its axis that separate the two regions of different wind stress curl polarity (negative southward and positive northward). The position of the GW seems to be constrained by this change of wind stress curl sign and is confined in the southern area [*Schott and McCreary*, 2001; *Beal et al*., 2013, their Figure 8]. The winds can also play a remote role in reinforcing the waves during their propagation across the Arabian basin [*Brandt et al*., 2002].

© 2014. American Geophysical Union. All Rights Reserved.

The GW has also been considered as a manifestation of the local western boundary current instability regime [*Wirth et al*., 2002]. The influence of the slanted coastline (roughly southwest-northeast) and the presence of Socotra Island on this regime have also been discussed in *McCreary and Kundu* [1988] and *Luther and O'Brien* [1989]. Their geomorphological constraint could also play a role in the steadiness of the eddy.

Finally, the collapse of the GW is not clear either. Prior to collapse, it sometimes moves southwestward seemingly under the influence of flanking cyclones before interacting with the equatorial dynamics [*Beal and Donohue*, 2013]. Other mechanisms have also been proposed such as internal instabilities [*Jensen*, 1993; *Wirth et al*., 2002] and merging with the Socotra Eddy, another remarkable steady anticyclonic eddy north of Socotra [*Fischer et al*., 1996].

In the present paper, we focus on the GW life cycle that is a key aspect of the mesoscale dynamics of the Arabian Sea, successively addressing the issues of generation, persistence, and collapse of the eddy. The use of a numerical model allows a consistent spatiotemporal view contrary to in situ measurements that are sparse in the region. In the next section, we present the model and the Arabian Sea configuration used here, along with a brief assessment of the simulation and a description of the seasonal dynamics as seen in the model. Then we focus on the GW life cycle before disentangling the role of remote versus local forcing on the regional dynamics using experiments that have been designed in such a way that those forcings can be independently switched off.

2. The ROMS Model

We use the version 3.0 of the Regional Ocean Modelling System - Agrif [ROMS, see *Shchepetkin and McWilliams*, 2005 for a complete description] (branch of ROMS developed by the Institut de Recherche pour le Développement [IRD] and INRIA; information can be found at http://www.romsagrif.org/). ROMS solves the primitive equations on an orthogonal curvilinear coordinates system. Its vertical component is terrain-following to better represent the effect of topography on the fluid. The advection scheme is third-order upstream-biased which acts as a subgrid-scale closure and allows not to add physical explicit eddy viscosity nor tracer diffusivity in the interior of the domain. The diffusive part of the advection scheme is rotated along the iso-geopotential surfaces to avoid spurious diapycnal mixing [*Marchesiello et al*., 2009]. Subgrid-scale vertical mixing processes are parameterized using the K-profile parameterization (KPP) boundary formulation [*Large et al*., 1994].

2.1. The Reference Arabian Sea Configuration

The grid has 640×640×56 points covering the Arabian Sea and a part of its adjacent seas, the Red Sea, and the Persian Gulf (10°S–28°N, 38.3°E–77.6°E, domain represented in Figure 2). The horizontal resolution is $1/16^\circ$ which corresponds to ∼6.6 km. We use stretching parameters θ_s=6.5 and θ_b=0 [*Haidvogel and Beckmann*, 1999] and the newly defined function of the vertical levels (Vtransform=2) which allows a more homogeneous distribution than the original function [*Lemarié et al*., 2012]. The minimum depth at which stretching occurs is defined with the parameter $h_c = 300$ m. It ensures a good representation of outflows in the shallow straits [depth less than 200 m, *Bower et al*., 2000] as well as in the interior basin. Bathymetry is taken from ETOPO2 data set [*Smith and Sandwell*, 1997]. It is smoothed under the constraint $\Delta h/2h < 0.2$ and the minimum depth represented is 15 m. Southern and eastern boundaries are open whereas northern (Persian Gulf) and western (Red Sea) boundaries are closed.

We use climatological forcing to investigate the proper seasonal and interannual variability of the ocean. Information on the data sets used for the forcing of the model and the validation is sum up in Table 1. Wind stress is taken from the Scatterometer Climatology of Ocean Winds (SCOW) data set [*Risien and Chelton*, 2008], computed on 122 months (September 1999 to October 2009) of QuikSCAT scatterometer data with a resolution of $1/4^\circ$. This climatology contains small-scale features [*Chelton et al*., 2004] such as island corner acceleration near Socotra Island and resolves the persistent influence of orography of the Arabian Peninsula and the Horn of Africa. Air-sea fluxes are taken from the in situ International Comprehensive Ocean Atmosphere Dataset (ICOADS) at $1/2^\circ$ of resolution [*Worley et al*., 2005]. Boundaries are forced with Simple Ocean Data Assimilation (SODA) data set release 2.1.6 [*Carton et al*., 2000]. To get temporal consistency between forcings, we computed a monthly climatology from this data set on nearly the same period as QuickSCOW.

© 2014. American Geophysical Union. All Rights Reserved.

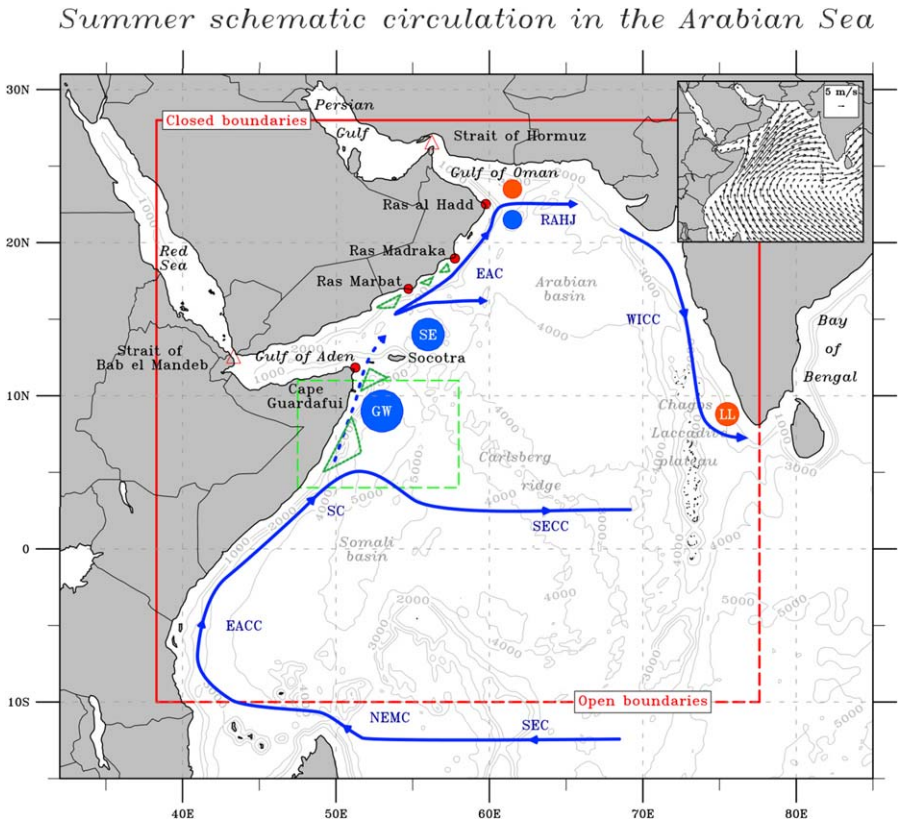

Figure 2. Schematic of the summer surface circulation in the Arabian Sea. The main source for the current paths is the reviews of *Schott and McCreary* [2001] and *Schott et al*. [2009] updated with *Beal et al*. [2013]. Green contoured wedges are the upwelling regions and blue (resp. orange) disks are nearly persistent anticyclones (resp. cyclones) during the SWM. The red lines represent the boundaries of the configuration used, plain lines are closed boundaries, and dashed lines are open boundaries. The inset at the top-right corner represents the climatological wind field in July at the peak of the SWM monsoon. The major currents and steady eddies are coarsely localized and abbreviated this way (from the north to the south): Ras Al Hadd Jet (RAHJ), East Arabian Current (EAC), West Indian Coastal Current (WICC), Socotra Eddy (SE), Great Whirl (GW), Laccadive Low (LL), Somalia Current (SC), South Equatorial Counter Current (SECC), East African Coastal Current (EACC), North East Madagascar Current (NEMC), and South Equatorial Current (SEC). The green dashed rectangle is the area over which surface kinetic energy is averaged in Figure 4c.

Table 1. Description of Data Sets Used for Forcing and Validation of the Model

Data Set	Resolution	Description
ETOPO2	1/30°	Global topography data set [*Smith and Sandwell*, 1997]. http://www.ngdc.noaa.gov/mgg/global/global.html
WOA09	1°	World Ocean Atlas, climatological fields of in situ temperature [*Locarnini et al*., 2010] and salinity [*Antonov et al*., 2010]. http://www.nodc.noaa.gov/OC5/WOA09/pr_woa09.html
SCOW	1/4°	Climatology of wind stress from QuickSCAT computed for the period September 1999 to October 2009 [*Risien and Chelton*, 2008]. Used to force the model. http://cioss.coas.oregonstate.edu/scow/
SODA	1/2°	Simple Ocean Data Assimilation data set, release 2.1.6 [*Carton et al*., 2000], climatology computed on the same period as SCOW. Used to force the model at open boundaries. http://soda.tamu.edu/data.htm
ICOADS	1/2°	International Comprehensive Ocean Atmosphere Dataset [*Worley et al*., 2005], in situ climatology. Air-sea fluxes used to force the model. http://icoads.noaa.gov/products.html
Aviso	1/3°	Absolute Dynamic Topography [*Rio and Hernandez*, 2004]. Variance computed for the same period as SCOW. http://www.aviso.oceanobs.com/en/data.html
OSTIA	1/20°	Operational Sea Surface Temperature and Sea Ice Analysis Seasonal climatology computed on period 2000–2008 [*Stark et al*., 2007] http://podaac.jpl.nasa.gov/dataset/UKMO-L4HRfnd-GLOB-OSTIA
GDP	1/2°	Global Drifter Program (Satellite-tracked surface drifting buoys) [*Lumpkin and Johnson*, 2013]. http://www.aoml.noaa.gov/phod/dac/index.php

© 2014. American Geophysical Union. All Rights Reserved.

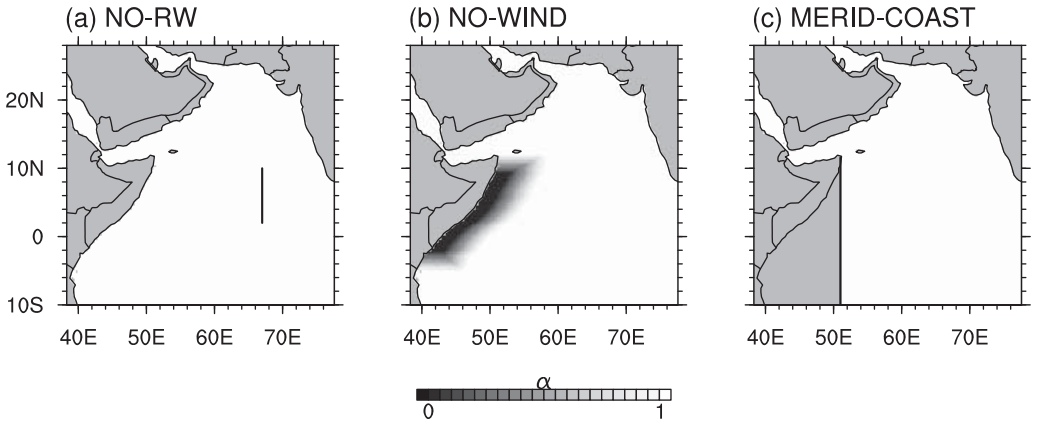

Figure 3. (a) The NO-RW domain with the wall in black line. (b) The damping function α by which is multiplied the reference wind stress in the domain for experiment NO-WIND (damping is linear). (c) The domain of the MERID-COAST experiment, black line is the new coastline.

The ocean is initially at rest, with temperature and salinity fields taken from the World Ocean Atlas 2009 data set [WOA09, *Antonov et al.*, 2010; *Locarnini et al.*, 2010] at 1° of resolution, in January (beginning of the simulation). This is our reference simulation (REF).

2.2. Sensitivity Experiments

In order to evaluate the impact of local and remote forcing on the GW life cycle, we set up sensitivity experiments to separate the role of different forcings. We ran each experiment for 10 years following 2 years of dynamical spin-up. All configuration parameters are identical to those of the reference simulation.

2.2.1. The NO-RW Experiment

The NO-RW experiment is designed to impede the propagation of long Rossby waves into the Arabian Sea by insulating the western basin from Rossby waves with a meridional wall at 67°E between 2°N and 10°N (Figure 3a). The physical consequence is the confinement of the western part of the basin from nearly any signal generated at the eastern side. Therefore, we ensure that the dynamics in the western Arabian Sea is nearly locally driven.

2.2.2. The NO-WIND Experiment

The NO-WIND experiment is designed to prevent the GW from being forced by local wind stress and wind stress curl (strongly negative) during the SWM (extended from May to September). The wind is linearly smoothed from its original value at 550 km (5° of longitude) from the coast to zero at 330 km (3° of longitude) from the coast. The smoothing is done over this relatively large area in order to avoid the creation of strong localized spurious Ekman pumping. The smoothing operator $\alpha(x, y, t)$ is defined as

$$(\tau^x_{\text{NO-WIND}}, \tau^y_{\text{NO-WIND}}) = \alpha \times (\tau^x_{\text{REF}}, \tau^y_{\text{REF}}), \quad (1)$$

(τ^x, τ^y) being the wind stress in the zonal and meridional directions. α is shown for the period May–September in Figure 3b.

2.2.3. The MERID-COAST Experiment

The influence of a slanted coastline on the reflection of waves at the western boundary and on the gyre circulation has been discussed by *Cane and Gent* [1984] and *McCreary and Kundu* [1988] but little has been said on its impact on the GW drift. To assess its importance, we set up the experiment MERID-COAST by setting a meridional coastline at the western boundary passing through Cape Guardafui (Figure 3c).

2.3. Evaluation of the Model and Description of the Basin Dynamics

Here we perform a comparison of the model solution with observed fields in order to evaluate the degree of confidence we can give to the diagnostics described further on. This includes an assessment of the Arabian Sea dynamics so as to better understand the processes governing the GW life cycle.

Figure 4 shows domain averaged kinetic energy at the surface and at 2000 m, and kinetic energy averaged near the western boundary encompassing the upwelling region (see legend for details). This is a good proxy to visualize the spin-up stage of the model. Starting from rest, we consider that the spin-up is done after

© 2014. American Geophysical Union. All Rights Reserved.

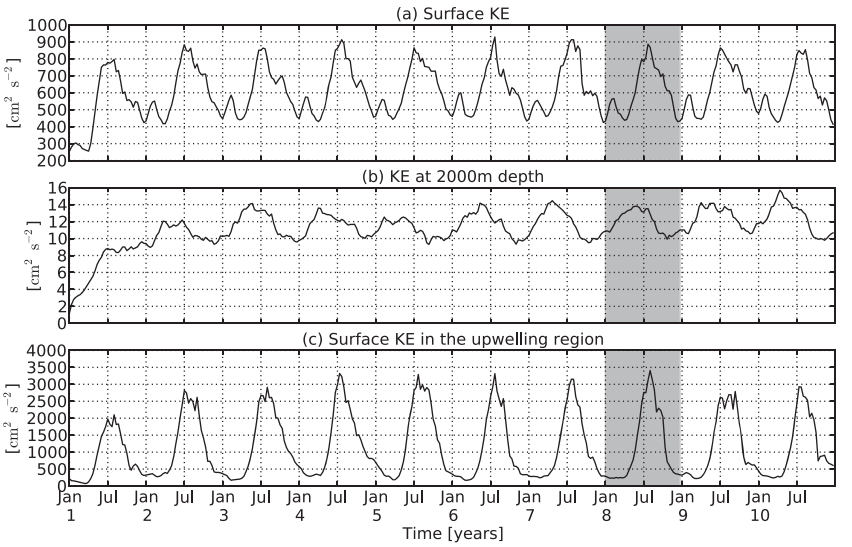

Figure 4. Kinetic energy (KE) averaged (a) at the surface on the whole domain, (b) at 2000 m depth on the whole domain, and (c) at the surface on the upwelling area marked in green dashed line in Figure 2. Year 8 is shadowed in gray to emphasize the normality of this year in terms of energetics as we take it to display typical scenario of the GW life cycle in Figure 8.

the first 2 years as there is no significant trend even at depth where the dynamics takes more time to reach an equilibrium. Consequently, all further diagnostics will be performed using the last 8 years of the simulation. Figure 4 also highlights a strong seasonal variability with the SWM (peak of the monsoon in July) dynamics being nearly twice as energetic as the NEM (centered in January) dynamics at the surface and even six times more energetic at the western boundary, consistent with a strong Ekman response to wind forcing [*Beal et al*., 2013]. The seasonal variability is also observed at 2000 m depth but with a less well-defined cycle. During the SWM, the kinetic energy extrema in the upwelling area (Figure 4c) arise at different dates and have different amplitudes depending on the year, although it should be noted that the forcing is climatological. This is due to intrinsic interannual variability associated with the chaotic nature of the forced turbulent flow [*Wirth et al*., 2002; *Penduff et al*., 2011].

As we noticed previously, the regional dynamics is highly seasonal due to the influence of monsoonal wind forcing. For this reason, we compute seasonal means based on the four periods NEM, SIM, SWM, and FIM, as commonly done in this region [e.g., *Resplandy et al*., 2011]. Figure 5 compares the climatology of Sea Surface Temperature (SST) computed over 8 years for the model with the SST from the Operational Sea Surface Temperature and Sea Ice Analysis product [OSTIA, *Stark et al*., 2007, see Table 1]. The OSTIA data set, delivered by the Met Office, has a horizontal resolution of $1/20^\circ$ and combines infrared and microwave satellites data as well as in situ data. Superimposed on these fields are the model and the *Lumpkin and Johnson* [2013] surface velocity climatologies (see Table 1). This data set uses quality controlled data from drogued drifters of the Global Drifter Program (GDP) from 1979 to June 2012. The general distribution of the model and OSTIA SSTs agree well in the interior of the domain during all seasons. The seasonal cycle is well represented in simulations north of 5°N, with large-scale patterns of colder SST during the NEM (a and b) and warmer SST during the SWM (e and f). This seasonal variability is seemingly driven by air-sea exchanges [*Vecchi et al*., 2004]. The coastal wind-driven upwellings off the Somali and Oman coasts [*Shi et al*., 2000] are spatially and seasonally consistent between model and observations during the SWM and the FIM. The minimum temperature in the Somali upwelling area is about 17°C, consistent with *Schott and McCreary* [2001]. The largest discrepancies appear in the adjacent seas during summer with a warm bias of the model of approximately 2°C. As these seas are not entirely represented in the domain, thermodynamical processes are partial and may account for those differences. Nonetheless, this may not influence much the inner dynamics of the Arabian Sea since the gulfs behind Hormuz and Bab El Mandeb straits, the Gulf of Oman and Gulf of Aden (see Figure 2 for geographical information), do not exhibit SST anomalies. The other bias appears at the equator during the SWM where the model surface water is approximately 1.5°C colder than the OSTIA SST. We diagnose that this anomaly comes from the open southern boundary according to the 3-D analysis of the velocity field.

© 2014. American Geophysical Union. All Rights Reserved.

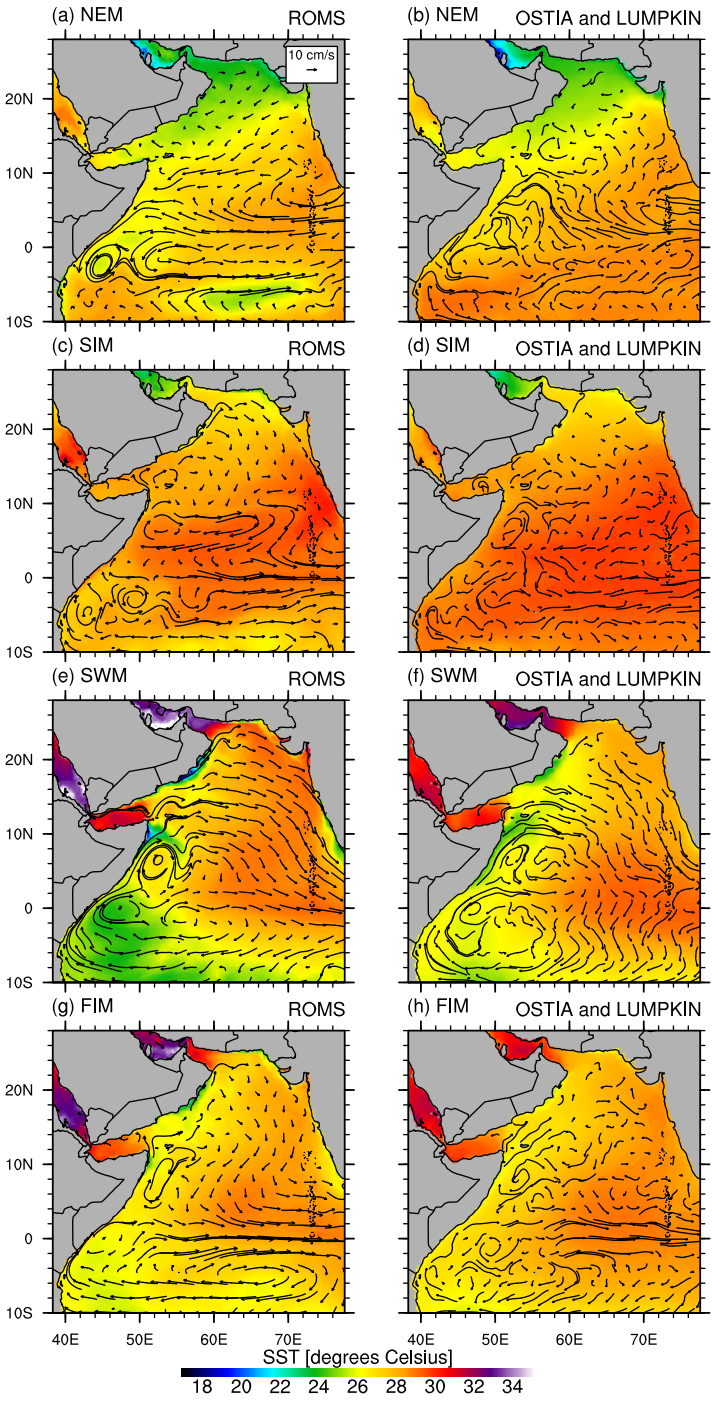

Figure 5. Climatology of Sea Surface Temperature (SST) and surface velocity computed for (left) the model and (right) OSTIA (SST) and the *Lumpkin and Johnson* [2013] surface drifter climatology for each season (from top to bottom: NEM, SIM, SWM, and FIM).

Because the Ekman component of the velocity is of primary importance in the Arabian Sea [*Hastenrath and Greischar*, 1991; *Beal et al*., 2013], we choose to compare the total velocity of the model with the observations rather than just the geostrophic component (derived from the sea surface height both in model and altimetry) as commonly done in model studies [e.g., *Mason et al*., 2011]. Another reason for this choice is that our model encompasses the equatorial band where estimating geostrophic velocity is difficult. To this end, we use the *Lumpkin and Johnson* [2013] surface drifter climatology that has been recently used in the region [*Beal et al*., 2013]. We find that the large-scale circulation agrees well during both monsoons, with the major zonal currents adequately represented. In addition to these qualitative comparisons, we compare the model SC structure with the equatorial observations of *Schott et al*. [1990]. Based on 2 years of an array of six moorings at 0° latitude between the coast and 175 km offshore, they computed a northward flow of 21 Sv ($1Sv=10^6 m^3 s^{-1}$) between the surface and 500 m for the period 1 June to 13 September. Taking the same area and time window, we find a SC mean transport of 23.1 Sv (std dev 3.2 Sv) for the 8 last years of simulation, in good agreement with *Schott et al*. [1990].

Mesoscale persistent structures at seasonal scales are effectively conserved in those climatologies, and the dominant imprint is the one of the GW close to the Somali coast at approximately 7°N during SWM. This is present in both the model and the in situ data, surrounded by a cold tongue of upwelled water [*Schott and McCreary*, 2001]. The model slightly overestimates horizontal velocities compared to drifter's climatology. This may partly be due to the low resolution of the latter (∼50km), for which mesoscale features are crudely resolved owing to a deformation radius of ∼140km in the region [*Chelton et al*., 1998]. The Southern Gyre [recirculation of the SC, *Schott et al*., 1990] south of the GW centered at the latitude of the equator is also represented in the model.

© 2014. American Geophysical Union. All Rights Reserved.

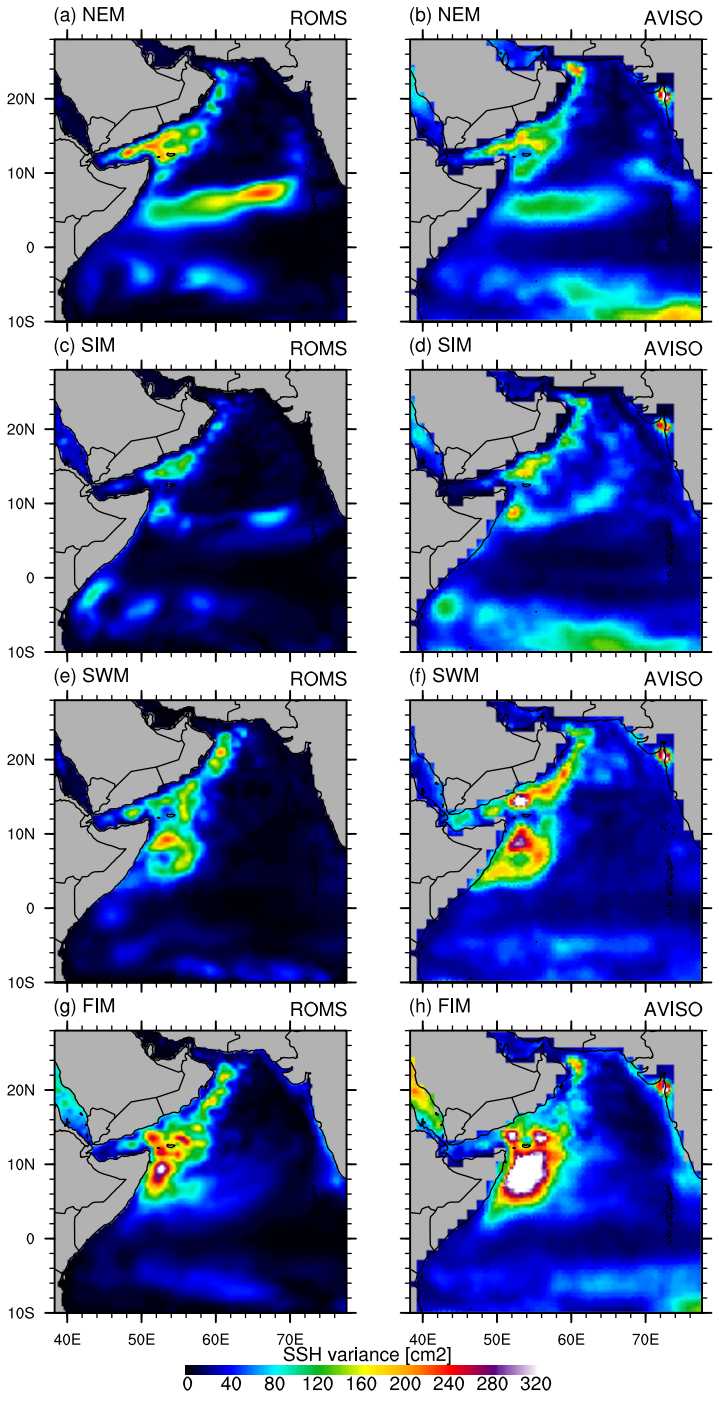

Figure 6. Sea surface height (SSH) variance for (left) the 8 years of simulation and (right) 10 years of MADT Aviso data (same period than the QuickSCOW climatology).

Figure 6 shows the sea surface height (SSH) variance computed over the last 8 years of the model simulation and the Aviso satellite altimetry-derived Absolute Dynamic Topography [ADP, *Rio and Hernandez*, 2004] variance computed on the same period as the SCOW wind forcing (Table 1). Here SSH variance is preferred over Eddy Kinetic Energy (EKE) because the geostrophic assumption [e.g., *Penven et al*., 2005] is not valid in part of our computation domain. Therefore, we rather use the SSH variance as an integrated proxy for available potential energy, thus EKE in a geostrophic turbulence framework [*Rhines*, 1979]. Global patterns show a strong seasonality that is very similar in the model and in the data except at latitudes south of 5°S, maybe due to inadequacies related to the forcing field at the southern boundary as previously noticed. We remark that for all seasons, the SSH variance is maximum at the western boundary, as expected from the basin large-scale circulation. During the NEM, the strong zonal strip of large SSH variance is consistent with the traveling of Rossby waves that emerges from the tip of India [*Brandt et al*., 2002], presumably created by a downwelling coastal Kelvin wave in the Bay of Bengal [*Rao et al*., 2010]. The SWM SSH variance underscores enhanced differences between the ocean interior and western boundary dynamics. The rapid onset of the SC is often interpreted in terms of reflection of long equatorial Rossby waves into short eastward Rossby waves [slowly propagating and accounting for the dynamics in a narrow coastal band, *Lighthill*, 1969; *Anderson and Gill*, 1975]. The enhanced energy level and variability can thus be attributed to Rossby wave-driven motions. The wind stress in the Arabian Sea is also found to be geographically and temporally at its peak (Figure 1). Hence, the wind work on the ocean circulation is maximum, implicitly forcing turbulent motions [*Hughes and Wilson*, 2008, and references therein]. The presence of a local minimum surrounded by a ring of elevated SSH variance reveals the position of the GW center which is relatively steady

© 2014. American Geophysical Union. All Rights Reserved.

over much of the SWM period. Model (7°17′N, 52°54′E) and data (6°53′N, 53°00′E) GW positions are in close agreement (the Aviso resolution at this latitude is ∼36km, thus the difference is of the order of one or two pixels), separated by approximately 45 km. Surprisingly, the largest pattern of SSH variance is reached during the FIM which is a season of low forcing by the wind, being a transition period between monsoons. SSH variance is representative of the level of geostrophic turbulence, itself essentially triggered by instability of the main currents [*Smith*, 2007]. During the SWM, seasonally steady currents set up and are fed by the constant wind stress field. After the end of the monsoon, the relaxing of the wind during the FIM leads to destabilization of the currents [*Lee et al*., 2000] thus to an enhancement of the geostrophic turbulence. SSH variance in our solution is generally lower than in the observations. We attribute this to the fact that interannual and intraseasonal (less than the monthly frequency) variabilities in the forcings (atmospheric and oceanic) are absent. Additional sources of variability would in particular contribute to displacements of the GW away from its mean location and enhance SSH variance levels in its vicinity.

We have also calculated EKE of the region and found high values within the upwelling area, reaching local values of 3000cm^{2}s^{-2} both in Aviso and the model, compatible with EKE generation of western boundary currents [*Ducet et al*., 2000]. As mentioned in section 1, this is substantially more than the EKE generated in the four major EBUS which is lower than 250cm^{2}s^{-2} [*Capet et al*., 2008]. Another particularity of this western boundary upwelling is that the maxima of EKE are very close to the coast (less than 100 km) whereas they are farther offshore in EBUS (more than 300 km from the coast). In the latter, the distance is attributed to the generation of small-scale eddy activity that undergoes an inverse cascade while moving westward, thus contributing to a maximum of geostrophic EKE offshore [*Kelly et al*., 1998]. In the Somali upwelling, eddying structures are prevented from moving westward by the coast, hence EKE remains concentrated nearshore.

This evaluation step helps us gain confidence in the realism of the simulated Arabian Sea circulation and eddy activity. Apart from discrepancies with observations near the southern boundary of the domain, the main large-scale currents are well represented and the global level of energy is consistent with satellite measurements. Importantly, excellent model-data agreement is achieved in terms of SSH variance patterns, including the location of the local minimum associated with the GW center (Figures 6e and 6f).

3. Dynamics of the Great Whirl

In this section, we describe the GW dynamics and show that it follows a well-defined life cycle on seasonal time scales, with some year-to-year variability, arising due to nonlinear interactions in our climatologically forced simulations [*Marchesiello et al*., 2003].

3.1. A Rossby Wave Linked With the Onset of the Great Whirl

We start by examining the remotely forced Rossby waves present in our reference simulation. Figures 7a, 7c, and 7e represent SSH at 7.5°N as a function of time and longitude in the model and in the observations. They reveal the clear annual propagation of planetary waves that have been identified as first and second baroclinic modes of long Rossby waves [*Subrahmanyam et al*., 2001] that are continuously reinforced by the wind while traveling along the basin [*Brandt et al*., 2002]. The typical phase speed in the model is 35cms^{-1}. It can be compared to the theoretical long Rossby wave speed c_ϕ:

$$c_\phi = -\beta R_d^2 = -\beta (c_1/f)^2 = -\frac{\beta}{\pi^2 f^2}\left(\int_{-H}^{0} N(z)\mathrm{d}z\right)^2 \quad (2)$$

where f and β are the planetary vorticity and its gradient, N is the Brunt-Vaisala frequency, and H is the ocean depth. $R_d = c_1/f$ is the first baroclinic Rossby radius of deformation where we use the WKB approximation to deduce the wave speed for c_1 [see e.g., *Chelton et al*., 1998]. Using equation (2), we find c_ϕ=44cms^{-1} which is close to the 38cms^{-1} found in *Brandt et al.* [2002] with the actual stratification. The discrepancy between the observed and the estimated model phase speed can be attributed to the modulation by the wind [*Subrahmanyam et al*., 2001], which can arise from the background flow velocity that induces a Doppler effect while propagating in the second half of the basin at the beginning of the SIM (Figure 5). The attenuation of the signal between 55°E and the coast is presumably related to the reflected signal into shorter waves which adds higher frequency noise to the original signal. In fact, according to *Cane and Gent* [1984], the long

© 2014. American Geophysical Union. All Rights Reserved.

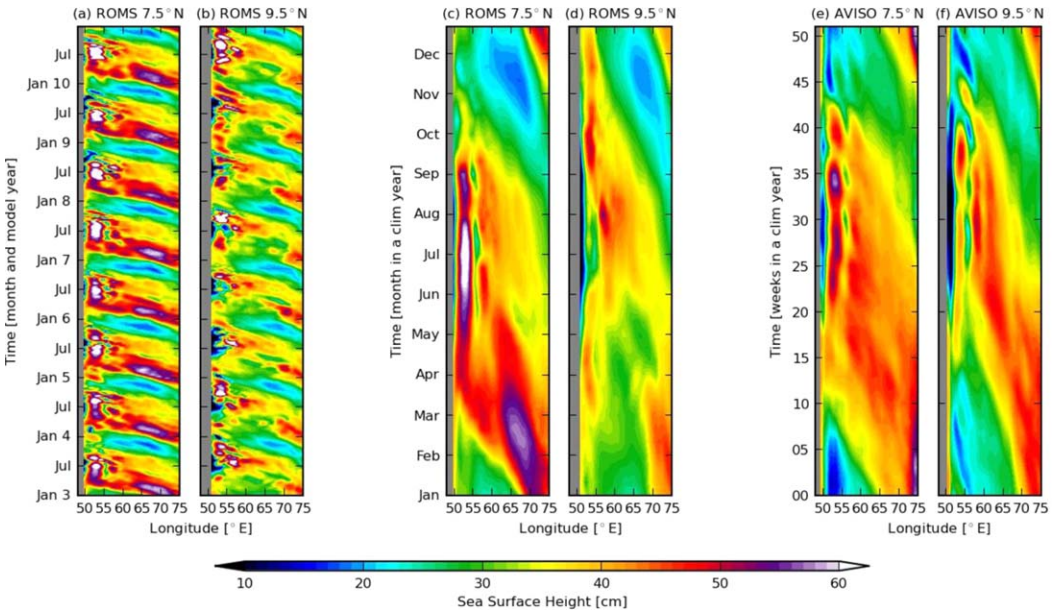

Figure 7. Hovmöller diagram of sea surface height (SSH) in the model at (a, c) 7.5°N and (b, d) 9.5°N on (Figures 7a, 7b) the last 8 years of simulation and (Figures 7c, 7d) for a climatological year (mean of years 3–8). (e, f) Aviso climatological SSH computed for years 1999–2009 (same period as forcing wind stress SCOW in the model). Aviso mean SSH has been shifted to match ROMS mean SSH to make plots comparable.

equatorial Rossby waves reaching a western boundary are reflected into eastward propagating Kelvin waves and short Rossby waves.

In this longitudinal band, we see during spring and summer the local maxima in SSH. In the interior of the basin, they are characteristic of downwelling Rossby waves, and at the coast from May to September it is the footprint of the GW. Although only qualitative, these elements indicate that our simulation produces realistic Rossby wave activity, the spring pulse being primarily generated by the eastern boundary condition with important modulations in the Arabian Sea.

3.2. Mature Stage of the Great Whirl

Figure 8 shows 10 day averaged SSH anomalies at different dates (on which the 10 day averages are centered) during year 8 of the simulation (whose energetics is comparable to the other years, as emphasized in the gray areas in Figure 4). It illustrates the typical scenario of the GW life cycle in the model, although there are some lags between different years in the various stages of the life cycle (onset, growth, and collapse), due to an intrinsic year-to-year variability. This figure can be examined alongside Figures 9 and 10 which present time series of the GW climatological attributes (latitude and longitude, SSH anomaly, radius, vorticity, and depth) in REF and the sensitivity runs. In this section, we focus on the REF simulation (black lines in Figures 9 and 10). The radius is computed by taking the area inside the contour of SSH anomaly of +6cm; then assuming that the GW geometry is circular, we obtain the equivalent radius. The choice of the contour ensures that a closed contour representative of the GW is defined at each time step. The value of the radius is therefore not absolute, as it depends on the chosen SSH level, but has a time-relative value that allows a quantitative comparison. The last feature displayed is the surface vertical relative vorticity $<\zeta> = <\partial_x v - \partial_y u>$, nondimensionalized by the local Coriolis frequency f, where $<\cdot> = \frac{1}{S}\int\int_S \cdot dS$ and S is the GW surface area (inside contour of SSH anomaly of 6 cm). The GW depth h is defined as being the depth at which the kinetic energy of the upper water column equals 75% of the kinetic energy of the whole water column:

$$\int_{-h}^{0} <\frac{1}{2}\mathbf{u}^2> dz = 0.75 \int_{-H}^{0} <\frac{1}{2}\mathbf{u}^2> dz \quad (3)$$

where H is the depth of the ocean and $\mathbf{u}=(u,v)$ is the horizontal velocity field. Again, h has no absolute signification but the 75% value has been chosen to ensure that the bulk of the eddy energy is captured. Superimposed with dashed line is the time-integrated Ekman pumping vertical velocity over the GW area:

© 2014. American Geophysical Union. All Rights Reserved.

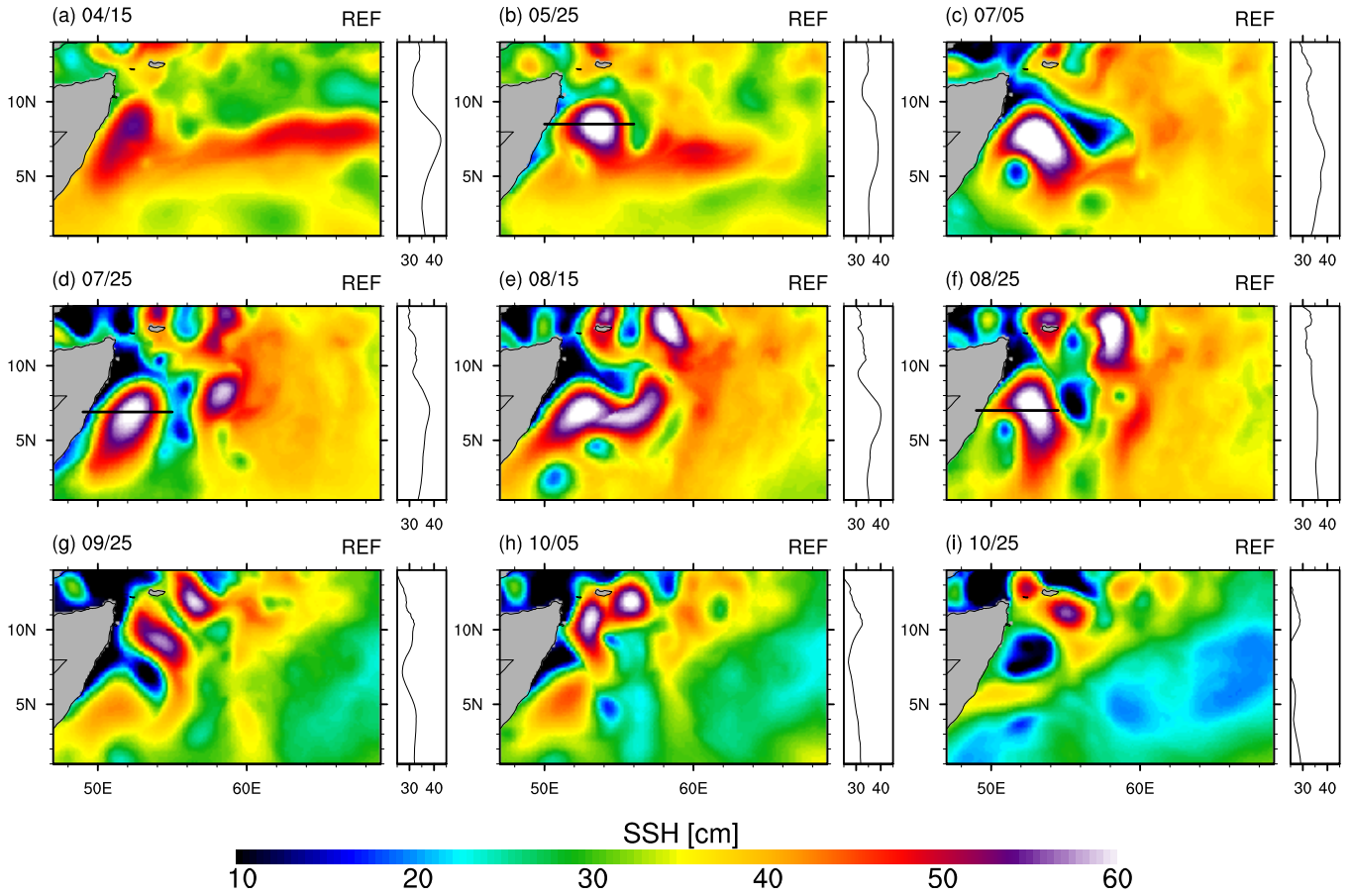

Figure 8. Sea surface height at year 8 averaged on 10 days centered on each date marked above figures. Zonal mean is computed for each figure and displayed on its right side. Black lines represent locations of sections in Figure 11. Colorbar is the same as Figure 7.

$$h_{Ek}(t) = \int_{t_0}^{t} \left[\frac{<\nabla \times \boldsymbol{\tau}(t')>}{\rho f_0} + \frac{\beta < \tau^x >}{\rho f_0^2} \right] dt' + h(t_0) \tag{4}$$

where $\boldsymbol{\tau} = (\tau^x, \tau^y)$ is the wind stress, ρ is the mean water density in the Ekman layer, and t_0 is 15 May. It corresponds to the depth of a layer forced solely by the Ekman pumping.

On 15 April (Figure 8a, on both the map and the zonal mean), we see the arrival of the Rossby wave at the coast, identified as a positive SSH anomaly roughly between 5°N and 10°N (also seen in Figures 7c and 7d). As mentioned before, the local SSH maximum around position (8°N, 52°E) is modulated by the superimposition of the incident and reflected waves. This is noticeable in Figures 7a and 7c in spring. From 25 May onward, the positive SSH anomaly seemingly trapped at the coast starts to swirl anticyclonically and gains negative vorticity (seen from 15 May onward in Figure 9e).

The GW reaches its most coherent state after the onset of the SWM at the beginning of June. On the 5 July snapshot, the eddy is seen in its commonly associated environment, flanked by two cyclones and by a cold filament of coastally upwelled water on its northern side [*Beal and Donohue*, 2013]. A close examination of the SSH field at a temporal resolution of 2 days (not shown) indicates that the flanking cyclones that surround the GW during the SWM originate from this mesoscale filament. The GW pulls the upwelled waters off the coast at its northern side, forming cyclones that detach from the pool of cold water as also observed in EBUS [*Mason et al.*, 2011, their Figure 7]. Their positions tend to evolve rapidly, and sometimes another anticyclone is found eastward of the GW on the other side of the cold wedge.

The Ekman forced depression of sea level at the coast (seen clearly on 25 July in Figure 8 as well as in Figures 7c and 7d) reveals the geostrophic path of the SC, flowing northeastward during the upwelling season of the SWM. The location of the GW is quasi-steady (Figures 9a and 9b) while its radius and its SSH

© 2014. American Geophysical Union. All Rights Reserved.

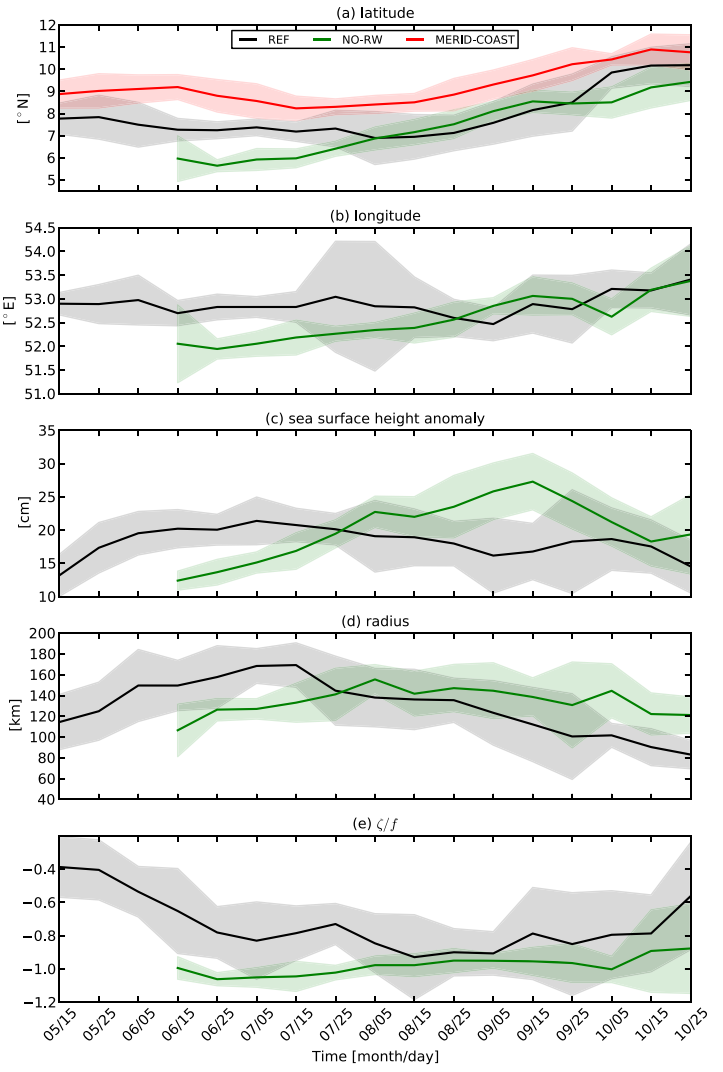

Figure 9. Temporal series of (a) latitude and (b) longitude of the Great Whirl center defined as the (c) local maximum of sea surface height anomaly, (d) radius, and (e) surface averaged relative vorticity nondimensionalized by the local Coriolis frequency. Shaded areas represent one standard deviation on each part of the mean. Standard deviation is computed by taking the biased estimator over eight realizations (8 years). Black line is for the REF simulation, green line for the NO-RW simulation, and red line for the MERID-COAST simulation.

anomaly increase until 5 July (Figures 9c and 9d), at which point they both start decreasing while the width to height aspect ratio of the GW remains relatively constant (not shown). The steadiness of this ratio is coherent with the constant surface velocity seen in Figure 11.

We see in the model the arrival of a second downwelling Rossby wave transporting another SSH maximum at 9.5°N (Figures 7b and 7d and in SSH zonal mean, Figures 8c–8e) in mid-July although it is not as clear in the data (Figure 7f). The presence of the wind curl maximum in this area (Figure 1) and at this time (Figure 10b, representative of the wind stress curl evolution in the GW vicinity) reinforces the positive anomaly at 57°E [as observed earlier in the season in *Brandt et al.*, 2002]. The highest interannual variability is found during this stage (largest standard deviation). We interpret this as a manifestation of the interannual variability of the Rossby wave itself (this is confirmed in further sensitivity experiment where Rossby waves are shut off). For instance, years 7 and 8 show a difference of 10cm in SSH (Figure 7), thus inducing different perturbations on the GW. Moreover, the SSH standard deviation also increases because of merging phenomena between anticyclones occurring at different times. The depth of the model GW dramatically increases from 50 m to 300 m, in agreement with the cruise observations of *Beal and Donohue* [2013] where the strongest surface intensified currents reach deeper than 200 m. This depth increase is also confirmed by the velocity and temperature sections of Figure 11. Thermal wind, deduced from the isopycnal slope, is observed to reach deep in the water column. We discuss the reasons accounting for this deepening in section 3.4.

During all years but one, the GW merges with the positive SSH anomaly (Figure 8e) that could be identified as the Socotra eddy [*Beal and Donohue*, 2013]. The resulting anticyclone migrates northward (Figure 9a, 15 August onward). The odd year displays a low decrease of the GW southward of the cold upwelling wedge, which seems to prevent northern merging. Even if the scenario described in this section is observed most of the years, lags exist between all these phases. The standard deviation from the mean accounts for this intrinsic interannual variability.

3.3. Dynamical Balance

It has been shown that, at a global scale [*Maximenko and Niiler*, 2006] and at a regional scale [*Penven et al.*, 2014], taking into account the effects of inertia reduce the error between geostrophic velocity from

© 2014. American Geophysical Union. All Rights Reserved.

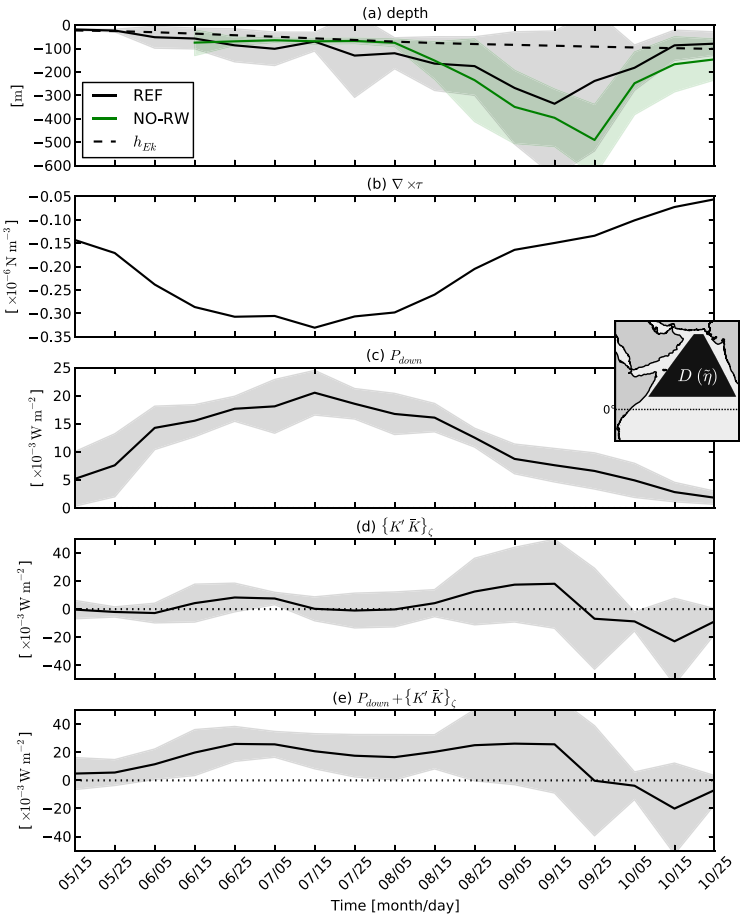

Figure 10. Temporal series of (a) depth (see text for computation), (b) wind stress curl averaged on the GW surface, (c) energy input by the wind acting to maintain the local anomaly of sea surface height [P_{down}, same notation as in *Roquet et al*., 2011], (d) transfer term between kinetic energy of the baroclinic flow and kinetic energy of the barotropic flow, and (e) is the sum of Figures 10c and 10d. Shaded areas represent one standard deviation on each part of the mean (biased estimator). Black line is for the REF simulation and green line for the NO-RW simulation. The dashed line in Figure 10a represents the deepening of the surface layer due to Ekman pumping (see text for details). The black trapezoid area on the inset map in Figure 10c is the area over which is computed the anomaly of sea surface height $\tilde{\eta}$.

altimetry and direct in situ measurements [as observed in *Fratantoni*, 2001]. In the case of anticyclonic eddies, neglecting inertia may lead to a 40% underestimate of the velocity [*Penven et al*., 2014]. The GW is nested in a western boundary where inertia is found to play a major role in dynamical balances. Moreover, nonlinear effects are expected to actively contribute to the dynamics as revealed by the local Rossby number $|\zeta/f|$, which is often greater than 0.5 during the GW life cycle (Figure 9e). Thus, we assess if the GW obeys a cyclostrophic regime (supposing axisymmetry of the eddy):

$$-fu_\theta = -g\frac{\partial \eta}{\partial r} + \frac{u_\theta^2}{r} \tag{5}$$

where u_θ is the azimuthal velocity, η is the SSH, r is the distance to the center of the eddy, and g is the acceleration of gravity.

Figure 12 shows the evolution of the different terms in equation (5) as well as the absolute value of the residual (i.e., $|-fu_\theta + g\partial\eta/\partial r - u_\theta^2/r|$). All terms are azimuthally averaged around the eddy center at each time step. The dominant balance all along the GW life cycle is geostrophic. However, the inertial term sometimes reaches 30% of either the Coriolis acceleration or the pressure gradient. This departure from geostrophy is to be expected considering the local Rossby number ($|\zeta/f| > 0.5$, Figure 9e). It is noticeable that all the terms are maximum around the peak of the monsoon when the wind stress curl is maximum (around 15 July, see Figure 10b). This adds support to a massive energy input into the GW by the wind stress curl, an assumption that will be tested in section 4.2.

© 2014. American Geophysical Union. All Rights Reserved.

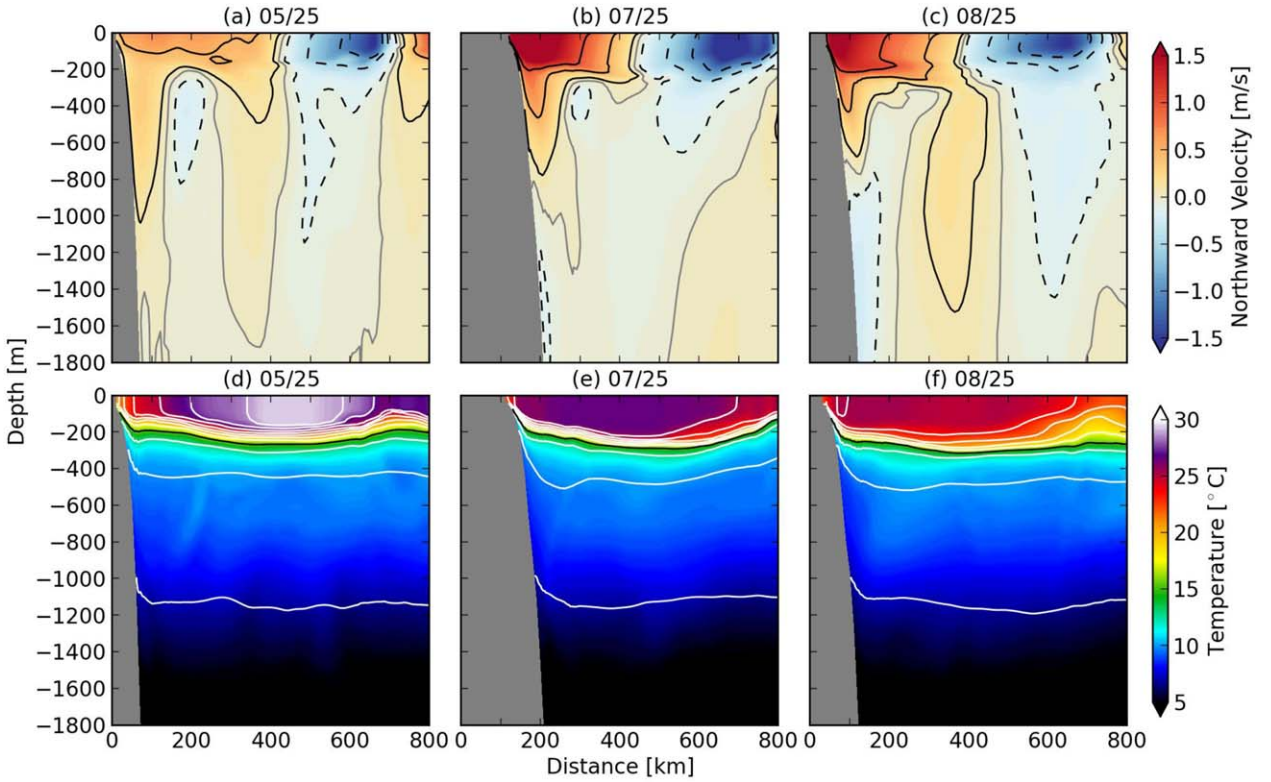

Figure 11. Velocity and temperature zonal sections in the Great Whirl core at locations of black lines in Figure 8. Black plain (resp. dashed) lines are contours of positive (resp. negative) velocity $\pm 0.1, 0.5, 1 \mathrm{ms}^{-1}$ around $0 \mathrm{ms}^{-1}$ gray line. White lines in temperature parts represent isopycnals with CI = 0.5.

Before September, the residual is less than 10% of the amplitude of the Coriolis acceleration within 250 km from the eddy center, thus confirming the validity of the cyclostrophic balance. Farther away, the hypothesis of axisymmetry is not necessarily valid and radial velocity may come into play in the balance. From the beginning of September onward, the residual slightly increases, sometimes being comparable to the inertial term. Although the main balance is still geostrophic, acceleration of velocity ($\partial u_\theta / \partial t$) may become important. This is consistent with the slowing down of the GW seen through the decrease in relative vorticity (Figure 9e).

3.4. Discussion on the Great Whirl Depth Evolution

We use the kinetic energy criterion (equation (3)) as a proxy to define the GW depth because it accurately reveals its deepening observed in sections such as shown in Figure 11. However, the reasons for the deepening observed during almost the whole eddy life cycle are not explained in the literature. In this section, we perform diagnostics on the wind input of energy to the GW and on internal kinetic energy transfers, then we comment on the mechanism of barotropization.

The wind can enhance the level of barotropic energy through wind work $\mathbf{u} \cdot \boldsymbol{\tau}$. Following *Roquet et al.* [2011], we compute the fraction of that wind work that contributes to maintaining (or producing) a local anomaly of sea surface height relative to its surrounding, and hence can reinforce the GW barotropic energy:

$$P_{down} = -\rho_0 g < \tilde{\eta}\, w_{Ek} > \tag{6}$$

where $w_{Ek} = \nabla \times \left(\frac{\tau}{\rho_0 f} \right)$ and $\tilde{\cdot}$ denotes a deviation from areal and yearly averaging performed over a domain D that covers our entire region of interest including that occupied by the GW at any given time (precisely D has a trapezoid shape defined by the vertices 24°N,63.4°E; 24°N,66.1°E; 4°N,76.1°E; 4°N,48.7°E, see inset map in Figure 10c). Results are not sensitive to the particular choice of D unless D is made so small that it only covers the GW area. Using sea level deviations from the areal mean over D ensures that the barotropic energy input we compute is not biased by the fact that w_{Ek} time and space averaged over our regional domain may not be exactly zero (computed over the entire domain D, P_{down} vanishes).

© 2014. American Geophysical Union. All Rights Reserved.

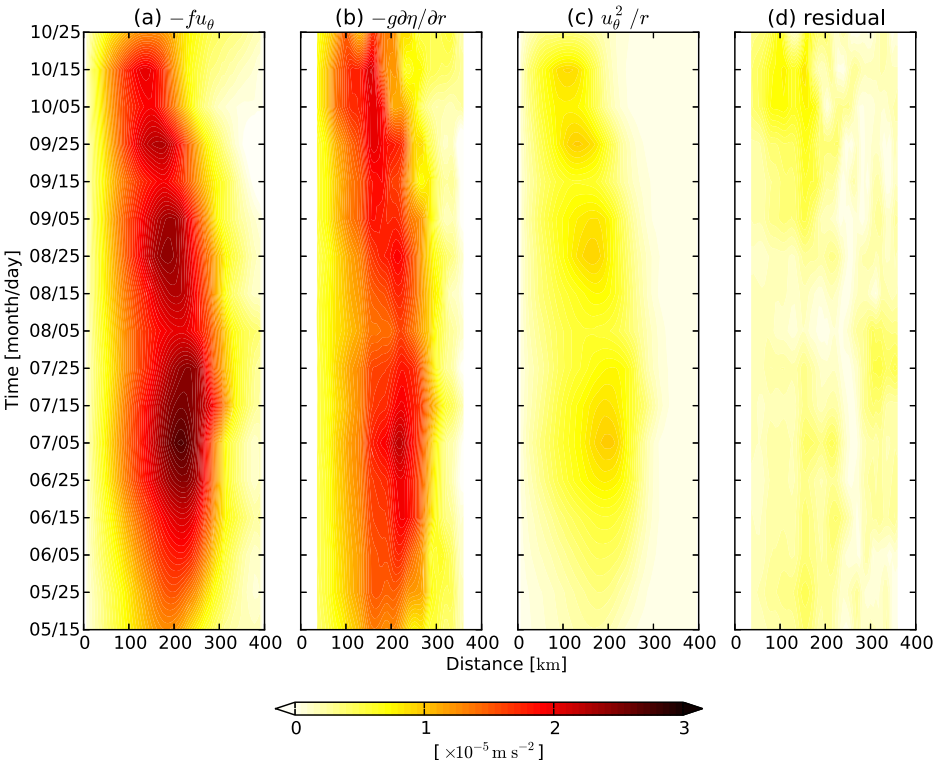

Figure 12. Different terms of the cyclostrophic balance (see equation (5)) azimuthally averaged around the GW center on years 2–8. (a) The Coriolis acceleration $-fu_\theta$, (b) the surface pressure gradient $-g\partial\eta/\partial r$, (c) the inertial term u_θ^2/r, and (d) the absolute residual $|-fu_\theta+g\partial\eta/\partial r-u_\theta^2/r|$. The derivative of SSH $\partial\eta/\partial r$ has been spatially low-pass filtered using a Lanczos filter with cutoff frequency at the grid scale to suppress noisy patterns due to differentiation.

Haney et al. [2001] studied the kinetic energy transformation between the vertical shear flow (i.e., baroclinic) and the vertical mean flow (i.e., barotropic) in California Current eddies. They find that these nonlinear processes of kinetic energy transformation are of crucial importance to account for the barotropization of eddies. The transformation of kinetic energy from the baroclinic flow (u', v') to the barotropic flow $(\bar{u}, \bar{v})$ can be written as follows:

$$\{K'\bar{K}\}=\{K'\bar{K}\}_\zeta+\{K'\bar{K}\}_\delta \tag{7}$$

with

$$\{K'\bar{K}\}_\zeta = \rho_0 H < \overline{\zeta'(\bar{u}v'-\bar{v}u')} > \tag{8}$$

$$\{K'\bar{K}\}_\delta = -\rho_0 H < \overline{\nabla\cdot\mathbf{u}(\bar{u}u'+\bar{v}v')} > \tag{9}$$

where H is still the total depth of the ocean and ρ_0 is a mean density. The overbar denotes a depth averaged quantity ($=\frac{1}{H}\int_{-H}^{0}\cdot dz$) and prime is the deviation from it. $\{K'\bar{K}\}_\zeta$ is the conversion term associated with the baroclinic vorticity and $\{K'\bar{K}\}_\delta$ is linked to the flow divergence. If $\{K'\bar{K}\} > 0$, kinetic energy is transferred from the baroclinic to the barotropic flow, thus increasing the deep ocean energy. When the flow obeys quasi-geostrophy, the exchange term associated with flow divergence ($\{K'\bar{K}\}_\delta$) is at least one order of magnitude smaller than the exchange term containing the relative vorticity ($\{K'\bar{K}\}_\zeta$). We also find this to be true for the GW, with mean values of $\{K'\bar{K}\}_\zeta$ around 4×10^{-3}Wm^{-2} and $\{K'\bar{K}\}_\delta$ smaller by a factor 11. Hence, we ignore $\{K'\bar{K}\}_\delta$ in our analysis.

Figures 10c and 10d show the time series of P_{down} and $\{K'\bar{K}\}_\zeta$, respectively, during the GW life cycle, i.e., the two key sources of energy for the barotropic mode. In Figure 10e, a strong correlation is found between the evolutions of the sum of both terms and GW depth: the deepening of the GW is associated with a plateau in the energy input (from 5 June to 15 September); then the reduction of the energy input coincides with a shallowing of the GW (presumably as a result of dissipation which we do not compute here).

© 2014. American Geophysical Union. All Rights Reserved.

Examination of the separate contribution of each term in the evolution of the GW depth suggests to consider two stages during the deepening of the eddy. First, from 15 May to 15 August, the depth increases with a rate compatible with the integrated Ekman pumping being the dominant driver (Figure 10a). P_{down} is greater than $\{K'\bar{K}\}_\zeta$, confirming the leading role of the wind stress curl in the deepening of the eddy. The second stage is from 15 August to 15–25 September where the GW keeps deepening (plausibly at a faster rate but the range of uncertainty is quite large) but with the baroclinic to barotropic kinetic energy conversion term as the dominant source of energy, especially in September.

From 25 September on, the GW suddenly shallows. P_{down} is still positive at this time but is small in amplitude compared to $\{K'\bar{K}\}_\zeta$ that is now negative, revealing an extraction of energy from the barotropic mode. *Wiin-Nielsen* [1962] gives a simple interpretation of the sign of this term using a two-layer quasi-geostrophic framework. When $\{K'\bar{K}\}_\zeta < 0$, there is warm advection in the region of cyclonic vorticity ($\zeta' > 0$) or cold advection in the region of anticyclonic vorticity ($\zeta' < 0$). Over the GW area, $\zeta' < 0$ in the surface layer, thus there must be an input of cold water in the GW area. It may not be coincidental that the rapid change of sign of $\{K'\bar{K}\}_\zeta$ takes place at the time of arrival of an upwelling Rossby wave (Figures 7c and 7d). We discuss this further in the following section.

Overall, we must recognize that these diagnostics offer a caveat in the interpretation due to the important error bar on $\{K'\bar{K}\}_\zeta$.

3.5. Collapse of the Great Whirl

The physical processes at play in the GW demise are still debated, as noted in section 1 (internal instability, merging, interaction with the equatorial band, etc.). The GW is commonly observable for more than a month after the monsoonal winds switch off at the end of September. This is also the case in the REF simulation for which the GW can be tracked until the end of October (Figure 9).

At the end of September, the GW has started weakening; its size and intensity jointly decrease while it moves northward at speed $\sim 7\text{km}\,\text{d}^{-1}$ (Figure 9) through advection by the SC, the interactions with surrounding eddies and the self-induced advection by interaction with the boundary (discussed in section 4.3). Its position is not limited by the zero wind curl line at this time as the Findlater jet is not active anymore during the FIM. The GW is also affected by an upwelling Rossby wave that reaches longitude 58°E and enters the GW influence area. It is noticeable in the Hovmöller diagram (Figures 7c and 7d) and signals concur between latitudes 7.5°N and 9.5°N [*Rao et al*., 2010]. Aviso data (Figures 7e and 7f) confirm the presence of this wave with very close timing and propagation speed, although amplitude is slightly reduced. At the beginning of October, this wave strengthens (Figures 8h and 8i, snapshot and zonal mean), imprinting a negative SSH anomaly shift to the entire zone, hence reducing the GW area and thus decreasing its radius. The propagation of this wave is closely observed in a 1993–2011 climatology of Aviso SSH anomaly in Figure 7c in *Beal et al*. [2013]. The characteristics of the GW show this loss of energy is through the damping of vorticity and the decrease of both the radius and the SSH anomaly. The upwelling triggered by this wave acts in favor of a shallowing of the eddy (Figure 10a). The Ekman depth does not evolve much and stays at the level it had at the end of the SWM, reflecting the inability of the wind to explain the eddy vertical extension at this stage. At the end of October, the Rossby wave has imposed a shift of roughly -5cm in SSH to the whole area (zonal means in Figures 8g–8i), which may contribute to the development of cyclonic eddies as seen on 25 October snapshot. The GW keeps shrinking and is not distinguishable after November for most of the years, in agreement with *Beal and Donohue* [2013].

Overall, our numerical solution suggests that the annual upwelling Rossby wave crossing the basin and reaching the coast during the FIM plays a crucial role in the GW collapse. We do not see in our model any sign of internal instability. The GW decays progressively toward the end of the SWM and somewhat more abruptly after the end of October, presumably under the influence of an upwelling Rossby wave. The weakening of the GW before the arrival of this wave is attributed to interactions with its highly turbulent environment which probably plays a role over the entire collapse period.

4. Local Versus Remote Forcing

We now further elaborate on the role of Rossby waves, local wind, and slanted coastline on the GW life cycle, especially on the generation and collapse mechanisms. We use the three sensitivity experiments presented in section 2.2 to isolate each of the effect.

© 2014. American Geophysical Union. All Rights Reserved.

As reviewed in section 1, there is no definite conclusion on the role of local (wind-induced eddy or current instability) and remote (planetary wave) forcing into the generation mechanisms. Before going into the results of the sensitivity experiments, we prior dismiss the possibility that parallel flow instabilities are implicated in the generation. When the GW is generated, there is no evidence in the model for a well-defined energetic current that could destabilize baroclinically. In fact, the SC starts to flow northward when the monsoonal winds start blowing, more than a month after the GW generation. We thus exclude baroclinic instability for the GW generation mechanism. This is consistent with *Smith* [2007] and *Tulloch et al*. [2011] who demonstrated that low-latitude flows are poorly inclined to baroclinic instability. Scaling analysis for the lateral shear maximum $U''_{\max}$ of the SC at 5°N at the end of May (during the generation stage of the GW) gives $U''_{\max} \sim 5 \times 10^{-12}\mathrm{m}^{-1}\mathrm{s}^{-1}$ while the β-effect modulated by the current orientation is $\beta\cos\phi = 1.5\times10^{-11}\mathrm{m}^{-1}\mathrm{s}^{-1}$, where $\phi \sim 45°$ is the angle between the current and the zonal direction. This indicates that the SC does not undergo a change of sign of $\beta\cos\phi - U''$. As such, the Rayleigh-Kuo inflection point criterion is not satisfied [e.g., *Vallis*, 2006] and the SC is not barotropically unstable at this time.

4.1. The NO-RW Experiment

The typical GW evolution in the NO-RW experiment is illustrated in Figures 13a–13f, again for year 8. On 15 April, we observe the blocking of the Rossby wave at the artificial wall, leaving a smoother SSH field on the western side in comparison with the REF simulation. At the beginning of July, 1 month after the onset of the monsoon, the anticyclonic structure that will evolve into the GW (Figure 13b, 5 July) has a shape resembling that for REF between 15 April and 25 May (Figures 8a and 8b). Therefore, the GW onset is delayed by approximately 2 months when Rossby waves are shut off. Statistically, the positive SSH anomaly gets its circular shape and starts swirling only around 15 June onward; we therefore calculate statistics for the NO-RW experiment from this date onward in Figure 9. This eddy is enhanced in its anticyclonic swirl (Figure 9e) by the wind curl, which provides negative vorticity throughout the SWM. During the following month, this anomaly strengthens and has roughly the same characteristics as in the REF simulation, albeit with a lag of 1–2 months in the GW life cycle (the lag slightly decreases as the season goes on).

During the growing phase, the position of the GW is also shifted ∼250 km to the southeast compared to REF. For this reason, we can unambiguously attribute the settlement of the GW at its characteristic position to the Rossby wave arrival at the coast. As a matter of fact, this phase-locking is absent in the NO-RW experiment, which explains the discrepancies. This is another argument in favor of the importance of this signal for the growth of the GW [supported by satellite observations of *Beal and Donohue*, 2013] against a wind-induced generation of the eddy.

A more general observation concerns the standard deviations of all the characteristics of the GW that are noticeably decreased in the NO-RW experiment compared to the REF simulation. As this simulation is to first order only forced by the wind west of the frontier, the fate of the GW is more deterministic, isolated from remotely forced signals which could perturb its life cycle. As a consequence, it keeps growing much longer than in REF. This is observed in the SSH anomaly and radius evolution (Figures 9c and 9d) that increase continuously under the influence of the wind without any merging or modulation by other signals. The vorticity is also higher and less variable than in REF as it is only forced by the local negative wind curl (this is likely linked with the slowly varying forcing [1 month of temporal resolution] and accounting for atmospheric synoptic variability could lead to smaller temporal scales in the ocean variability [*Desbiolles et al*., 2014]) (Figure 9e). As standard deviations in the time series account for the interannual variability (deviation from the climatological mean), we attribute a strong part of year-to-year variability of the GW to the Rossby waves.

The GW collapse is also observed later because the eddy is not perturbed by the incoming upwelling Rossby wave emerging from the east of the basin. It should be noted that the blocking of this wave appears to be only partial (Figures 13e–13f), but it delays and strongly reduces the amplitude of the wave. The GW is still observable on snapshot 5 November and eventually disappears 20–30 days later than in REF. Furthermore, Figures 9c, 9d, and 9e demonstrate that the GW in NO-RW is stronger than in REF during its last month of existence (i.e., October). This behavior confirms that Rossby wave dynamics have a major impact on the GW collapse.

4.2. The NO-WIND Experiment

This experiment shows reduced interannual variability and a less intense coastal forcing, promoting a more linear response of the ocean over a wide area. The basic scenario is displayed in Figures 13g–13i. The

© 2014. American Geophysical Union. All Rights Reserved.

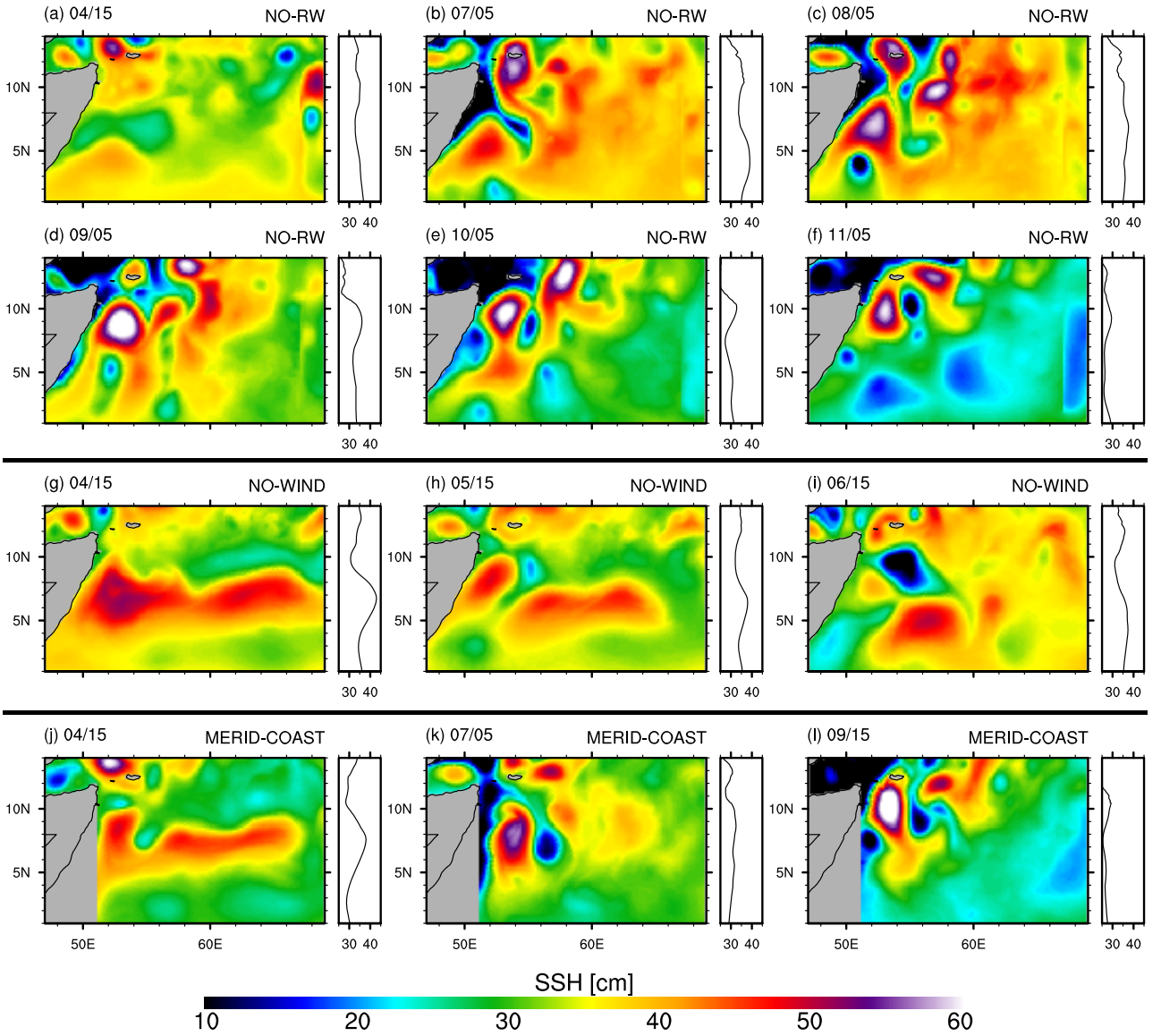

Figure 13. Same as Figure 8 but for experiments (a–f) NO-RW, (g–i) NO-WIND, and (j–l) MERID-COAST.

Rossby wave signal, identified through a local maximum of SSH, reaches the coast between the end of March and the beginning of April, before swirling anticyclonically close to the coast to become the GW. Until mid-April, there is no qualitative difference between the REF and NO-WIND mean ocean states. General patterns of the snapshot on 15 April (Figures 8a and 13g) are very similar. Differences occur after mid-May as the wind is damped sufficiently. The enhancement of the Rossby wave by the wind does not occur and the signal gradually attenuates until reaching the coast. Therefore, we observe a decrease in the GW intensity before its rapid disappearance among other ephemeral small eddying patterns. This highlights the role of the local winds as a source of negative vorticity driving the evolution of the GW and in particular its growth. Incidentally, statistics cannot easily be computed for the more diffuse shape of the GW (as done for REF and NO-RW, see Figure 9). The strong negative SSH anomaly visible on 15 June (Figure 13i) is the consequence of the wind damping which occurs a 100 km offshore of this anomaly. In this situation, the cyclone is reinforced by the positive wind curl artificially induced by the damping.

4.3. The MERID-COAST Experiment

Once generated and stabilized by the monsoonal winds, the GW remains quasi-stationary during more than 3 months. This temporal and geographical steadiness is unusual and does not occur in the open ocean as

© 2014. American Geophysical Union. All Rights Reserved.

the longest satellite-tracked eddies always move westward [*Chelton et al*., 2007]. The local geomorphology with the almost 45°-oriented coastline could influence the eddy drift as modeled by *McCreary and Kundu* [1988] in a very simplified numerical setup.

Eddy drift is determined by several processes: (i) the westward dominated drift at the long Rossby wave speed βR_d^2, modulated by an equatorward (resp. poleward) deflection for anticyclones (resp. cyclones) [*Morrow et al*., 2004]; (ii) advection by the mean currents; (iii) interactions with surrounding eddies [e.g., *Carton*, 2001], and (iv) self-induced advection by interaction with a boundary in the vicinity of a coast [e.g., *Carton et al*., 2013]. The GW is subject to all of these processes and the slant of the coast relative to the meridional direction primarily affects (i) and (iv). The MERID-COAST experiment is designed to assess the relative importance of this slanted coastline.

Figure 9a shows the climatological latitude of the GW in the MERID-COAST experiment. Longitude is not presented because it is overly affected by the coastline modification and therefore not comparable with the other experiments. The GW position is shifted to the north by approximately 1.5° from the REF experiment but undergoes the same northward translation from August onward. The Rossby wave reaches the coast further north than in REF, thus also settling the GW position northward. However, it obviously does not affect the fate of the eddy drift. Hence, we conclude that the slanted coastline has a limited impact on the GW drift.

Interestingly, MERID-COAST confirms that until the end of the monsoonal winds in early September, the northern flank of the GW cannot cross the zero wind curl line. Therefore, this certainly accounts for the steadiness of the GW position during the monsoon, regardless of fluctuations attributed to eddy-eddy interactions. After the end of the monsoon, the GW is more isolated and its northward drift is more likely due to a combination of advection by the SC and self-advection of the eddy by interacting with the boundary; (ii) and (iv) becoming the dominant processes among those enumerated in the preceding paragraph.

5. Summary

In this paper, we presented a ROMS regional simulation of the Arabian Sea circulation, climatologically forced at a horizontal resolution allowing for an adequate representation of mesoscale dynamics. After approximately 2 years, the model reaches statistical equilibrium and exhibits a marked interannual variability of intrinsic origin. Overall, the characteristic seasonality of the regional dynamics due to monsoonal winds in the Indian Ocean is well represented in the model. This therefore gives us confidence in the model for use to investigate the southwest monsoon dynamics, particularly its dominant mesoscale structure, the GW.

We precisely characterize the life cycle of the GW. We confirm the preconditioning effect of an annual downwelling Rossby wave. This wave exerts a major influence on the GW initial phase (location and timing of initiation), as suggested by *McCreary et al*. [1993] and observed by *Beal and Donohue* [2013]. The roles of the strong wind stress and anticyclonic wind stress curl remain crucial to explain the maintenance and the barotropization of the eddy. In fact, we found that although the strong Ekman pumping can explain the deepening of the eddy during the early stage of the monsoon, nonlinear kinetic energy transfer from the baroclinic flow to the barotropic flow may come into play to redistribute the input of surface energy by the wind stress curl into the deeper layers. The sudden shallowing of the GW at the end of its life cycle is compatible with the arrival of an upwelling Rossby wave. Nonetheless, this diagnostic of kinetic energy transfer appeared to be difficult to interpret in terms of water mass exchanges as proposed by *Wiin-Nielsen* [1962] and *Haney et al*. [2001] and investigation on the GW deepening is not closed.

An examination of the different terms constituting the cyclostrophic balance reveals that inertia is important for the GW dynamical structure, reaching 30% of the geostrophic terms.

The GW sits in a very turbulent western boundary upwelling region and detaches cyclones from the northern cold filament of upwelled water that circles it. Cyclones move around it and interact, leading to intraseasonal and interannual variability in its position. After the shutoff of the monsoonal winds, the GW starts to shrink during the FIM when the EKE is found to be at its peak, revealing a strongly turbulent environment. It is then mainly influenced by its interaction with surrounding eddies and the coast and self-induced advection by interaction with the boundary, causing it to drift northward. The arrival of an annual upwelling

© 2014. American Geophysical Union. All Rights Reserved.

Rossby wave at the end of October causes the collapse of the GW, which then dramatically shrinks and finally disappears.

A parallel could be made with the Loop Current Eddies where a dominant anticyclone dominates a turbulent environment made of smaller cyclones. As in the study of *Chérubin et al*. [2006], we suggest that the stability of the GW and its interaction with surrounding eddies could be studied by taking into account its baroclinic structure.

Sensitivity tests confirm the importance of Rossby waves to pace the GW life cycle. When Rossby waves are shut off, the GW onset is delayed by almost 2 months and its position is shifted by ∼250 km southward. The GW collapse is also delayed by approximately 1 month. The role of these waves has been generally underestimated in comparison to the role of local high winds. However, their importance in interacting with eddies is not that surprising since *Polito and Liu* [2003] qualified the annual and semiannual Rossby waves are among the most energetic of the planetary waves. However, when the wind is shut off, the GW disappears rapidly after its onset. This also confirms the crucial importance of the wind stress and wind stress curl to energetize the GW. Finally, the role of the slanted coastline is found to be negligible in the GW drift as the eddy gradually undergoes the same northward translation as modeled in the reference experiment.

Acknowledgments
The authors are grateful to A. Colin de Verdière (LPO, UBO) for the instructive comment on the wave-driven dynamical adjustment to the monsoon onset. All data set used in this work were downloaded from the internet addresses mentioned in Table 1. Simulations were performed on the computing center Caparmor at Ifremer. CV is supported by the Direction Générale de l'Armement (DGA) and the Région Bretagne in the form of a PhD scholarship. This study is a contribution to the French ANR Synbios. The authors also acknowledge Matthew Thomas (LPO, Ifremer) for his comments and corrections and two anonymous reviewers for their thorough remarks.

References

Anderson, D. L., and A. Gill (1975), Spin-up of a stratified ocean, with applications to upwelling, *Deep Sea Res. Oceanogr. Abstr.*, *22*(9), 583–596.
Antonov, J., D. Seidov, T. Boyer, R. Locarnini, A. Mishonov, H. Garcia, O. Baranova, M. Zweng, and D. Johnson (2010), *World Ocean Atlas 2009,* vol. 2, *Salinity*, *NOAA Atlas NESDIS 69*, U.S. Gov. Printing Office, Washington, D. C.
Beal, L., and K. Donohue (2013), The Great Whirl: Observations of its seasonal development and interannual variability, *J. Geophys. Res. Oceans*, *118*, 1–13, doi:10.1029/2012JC008198.
Beal, L., V. Hormann, R. Lumpkin, and G. Foltz (2013), The response of the surface circulation of the Arabian Sea to monsoonal forcing, *J. Phys. Oceanogr.*, *43*(9), 2008–2022, doi:10.1175/JPO-D-13-033.1.
Bower, A. S., H. D. Hunt, and J. F. Price (2000), Character and dynamics of the Red Sea and Persian Gulf outflows, *J. Geophys. Res.*, *105*(C3), 6387–6414, doi:10.1029/1999JC900297.
Brandt, P., L. Stramma, F. Schott, J. Fischer, M. Dengler, and D. Quadfasel (2002), Annual Rossby waves in the Arabian Sea from TOPEX/POSEIDON altimeter and in situ data, *Deep Sea Res., Part II*, *49*(7), 1197–1210, doi:10.1016/S0967-0645(01)00166-7.
Bruce, J. (1983), The wind field in the western Indian Ocean and the related ocean circulation, *Mon. Weather Rev.*, *111*(7), 1442–1452.
Cane, M. A., and P. R. Gent (1984), Reflection of low-frequency equatorial waves at arbitrary western boundaries, *J. Mar. Res.*, *42*(3), 487–502.
Capet, X., F. Colas, J. McWilliams, P. Penven, and P. Marchesiello (2008), Eddies in eastern boundary subtropical upwelling systems, in *Ocean Modeling in an Eddying Regime*, edited by M. W. Hecht and H. Hasumi, pp. 131–147, AGU, Washington, D. C., doi:10.1029/177GM10.
Carton, J., G. Chepurin, X. Cao, and B. Giese (2000), A simple ocean data assimilation analysis of the global upper ocean 1950-95. Part I: Methodology, *J. Phys. Oceanogr.*, *30*(2), 294–309.
Carton, X. (2001), Hydrodynamical modeling of oceanic vortices, *Surv. Geophys.*, *22*(3), 179–263, doi:10.1023/A:1013779219578.
Carton, X., B. Le Cann, A. Serpette, and J. Dubert (2013), Interactions of surface and deep anticyclonic eddies in the Bay of Biscay, *J. Mar. Syst.*, *109*, S45–S59.
Chelton, D., R. DeSzoeke, M. Schlax, K. El Naggar, and N. Siwertz (1998), Geographical variability of the first baroclinic Rossby radius of deformation, *J. Phys. Oceanogr.*, *28*(3), 433–460.
Chelton, D., M. Schlax, M. Freilich, and R. Milliff (2004), Satellite measurements reveal persistent small-scale features in ocean winds, *Science*, *303*(5660), 978–983, doi:10.1126/science.1091901.
Chelton, D. B., M. G. Schlax, R. M. Samelson, and R. A. de Szoeke (2007), Global observations of large oceanic eddies, *Geophys. Res. Lett.*, *34*, L15606, doi:10.1029/2007GL030812.
Chérubin, L. M., Y. Morel, and E. P. Chassignet (2006), Loop Current ring shedding: The formation of cyclones and the effect of topography, *J. Phys. Oceanogr.*, *36*(4), 569–591, doi:10.1175/JPO2871.1.
Desbiolles, F., B. Blanke, and A. Bentamy (2014), Short-term upwelling events at the western African coast related to synoptic atmospheric structures as derived from satellite observations, *J. Geophys. Res. Oceans*, *119*, 461–483, doi:10.1002/2013JC009278.
Ducet, N., P.-Y. Le Traon, and G. Reverdin (2000), Global high-resolution mapping of ocean circulation from TOPEX/Poseidon and ERS-1 and-2, *J. Geophys. Res.*, *105*(C8), 19,477–19,498, doi:10.1029/2000JC900063.
Findlater, J. (1969), A major low-level air current near the Indian Ocean during the northern summer, *Q. J. R. Meteorol. Soc.*, *95*(404), 362–380, doi:10.1002/qj.49709540409.
Fischer, J., F. Schott, and L. Stramma (1996), Currents and transports of the Great Whirl-Socotra Gyre system during the summer monsoon, August 1993, *J. Geophys. Res.*, *101*(C2), 3573–3587, doi:10.1029/95JC03617.
Fratantoni, D. M. (2001), North Atlantic surface circulation during the 1990's observed with satellite-tracked drifters, *J. Geophys. Res.*, *106*(C10), 22,067–22,093.
Haidvogel, D. B., and A. Beckmann (1999), *Numerical Ocean Circulation Modeling*, vol. 344, Imp. Coll. Press, London, U. K.
Haney, R. L., R. A. Hale, and D. E. Dietrich (2001), Offshore propagation of eddy kinetic energy in the California Current, *J. Geophys. Res.*, *106*(C6), 11,709–11,717.
Hastenrath, S., and L. Greischar (1991), The monsoonal current regimes of the tropical Indian Ocean: Observed surface flow fields and their geostrophic and wind-driven components, *J. Geophys. Res.*, *96*(C7), 12,619–12,633, doi:10.1029/91JC00997.
Hughes, C. W., and C. Wilson (2008), Wind work on the geostrophic ocean circulation: An observational study of the effect of small scales in the wind stress, *J. Geophys. Res.*, *113*, C02016, doi:10.1029/2007JC004371.
Jensen, T. G. (1993), Equatorial variability and resonance in a wind-driven Indian Ocean model, *J. Geophys. Res.*, *98*(C12), 22,533–22,552, doi:10.1029/93JC02565.

© 2014. American Geophysical Union. All Rights Reserved.

Kelly, K. A., R. C. Beardsley, R. Limeburner, K. H. Brink, J. D. Paduan, and T. K. Chereskin (1998), Variability of the near-surface eddy kinetic energy in the California Current based on altimetric, drifter, and moored current data, *J. Geophys. Res.*, *103*(C6), 13,067–13,083.
Kim, H.-S., C. N. Flagg, and S. D. Howden (2001), Northern Arabian Sea variability from TOPEX/POSEIDON altimetry data: An extension of the US JGOFS/ONR shipboard ADCP study, *Deep Sea Res., Part II*, *48*(6), 1069–1096, doi:10.1016/S0967-0645(00)00131-4.
Large, W., J. McWilliams, and S. Doney (1994), Oceanic vertical mixing: A review and a model with a nonlocal boundary layer parameterization, *Rev. Geophys.*, *32*(4), 363–403, doi:10.1029/94RG01872.
Lee, C., B. Jones, K. Brink, and A. Fischer (2000), The upper-ocean response to monsoonal forcing in the Arabian Sea: Seasonal and spatial variability, *Deep Sea Res., Part II*, *47*(7), 1177–1226, doi:10.1016/S0967-0645(99)00141-1.
Leetmaa, A., D. Quadfasel, and D. Wilson (1982), Development of the flow field during the onset of the Somali Current, 1979, *J. Phys. Oceanogr.*, *12*(12), 1325–1342.
Lemarié, F., J. Kurian, A. F. Shchepetkin, M. Jeroen Molemaker, F. Colas, and J. C. McWilliams (2012), Are there inescapable issues prohibiting the use of terrain-following coordinates in climate models?, *Ocean Modell.*, *42*, 57–79.
Lighthill, M. J. (1969), Dynamic response of the Indian Ocean to onset of the southwest monsoon, *Philos. Trans. R. Soc. London A*, *265*(1159), 45–92, doi:10.1098/rsta.1969.0040.
Locarnini, R., A. Mishonov, J. Antonov, T. Boyer, H. Garcia, O. Baranova, M. Zweng, and D. Johnson (2010), *World Ocean Atlas 2009,* vol. 1, *Temperature*, U.S. Gov. Print. Off., Washington, D. C.
Lumpkin, R., and G. C. Johnson (2013), Global ocean surface velocities from drifters: Mean, variance, El Nino–Southern Oscillation response, and seasonal cycle, *J. Geophys. Res. Oceans*, *118*, 2992–3006, doi:10.1002/jgrc.20210.
Luther, M. E., and J. J. O'Brien (1989), Modelling the variability in the Somali Current, in *Mesoscale/Synoptic Coherent Structures in Geophysical Turbulence*, pp. 373–386, Elsevier, Amsterdam.
Marchesiello, P., J. McWilliams, and A. Shchepetkin (2003), Equilibrium structure and dynamics of the California Current System, *J. Phys. Oceanogr.*, *33*(4), 753–783.
Marchesiello, P., L. Debreu, and X. Couvelard (2009), Spurious diapycnal mixing in terrain-following coordinate models: The problem and a solution, *Ocean Modell.*, *26*(3), 156–169, doi:10.1016/j.ocemod.2008.09.004.
Mason, E., F. Colas, J. Molemaker, A. F. Shchepetkin, C. Troupin, J. C. McWilliams, and P. Sangrà (2011), Seasonal variability of the Canary Current: A numerical study, *J. Geophys. Res.*, *116*, C06001, doi:10.1029/2010JC006665.
Maximenko, N., and P. Niiler (2006), Mean surface circulation of the global ocean inferred from satellite altimeter and drifter data, paper presented at Symposium on 15 Years of Progress in Radar Altimetry, European Space Agency Spec. Publ., ESA Publication Division, Noordwijk, Netherlands.
McCreary, J., and P. Kundu (1988), A numerical investigation of the Somali Current during the Southwest Monsoon, *J. Mar. Res.*, *46*(1), 25–58, doi:10.1357/002224088785113711.
McCreary, J., P. Kundu, and R. Molinari (1993), A numerical investigation of dynamics, thermodynamics and mixed-layer processes in the Indian Ocean, *Prog. Oceanogr.*, *31*(3), 181–244, doi:10.1016/0079-6611(93)90002-U.
Morrow, R., F. Birol, D. Griffin, and J. Sudre (2004), Divergent pathways of cyclonic and anti-cyclonic ocean eddies, *Geophys. Res. Lett.*, *31*, L24311, doi:10.1029/2004GL020974.
Penduff, T., M. Juza, B. Barnier, J. Zika, W. K. Dewar, A.-M. Treguier, J.-M. Molines, and N. Audiffren (2011), Sea level expression of intrinsic and forced ocean variabilities at interannual time scales, *J. Clim.*, *24*(21), 5652–5670.
Penven, P., V. Echevin, J. Pasapera, F. Colas, and J. Tam (2005), Average circulation, seasonal cycle, and mesoscale dynamics of the Peru Current System: A modeling approach, *J. Geophys. Res.*, *110*, C10021, doi:10.1029/2005JC002945.
Penven, P., I. Halo, S. Pous, and L. Marié (2014), Cyclogeostrophic balance in the Mozambique Channel, *J. Geophys. Res. Oceans*, *119*, 1054–1067, doi:10.1002/2013JC009528.
Polito, P. S., and W. T. Liu (2003), Global characterization of Rossby waves at several spectral bands, *J. Geophys. Res.*, *108*(C1), 3018, doi:10.1029/2000JC000607.
Rao, R., G. Kumar, M. Ravichandran, A. Rao, V. Gopalakrishna, and P. Thadathil (2010), Interannual variability of Kelvin wave propagation in the wave guides of the equatorial Indian Ocean, the coastal Bay of Bengal and the southeastern Arabian Sea during 1993–2006, *Deep Sea Res., Part I*, *57*(1), 1–13, doi:10.1016/j.dsr.2009.10.008.
Resplandy, L., M. Lévy, G. Madec, S. Pous, O. Aumont, and D. Kumar (2011), Contribution of mesoscale processes to nutrient budgets in the Arabian Sea, *J. Geophys. Res.*, *116*, C11007, doi:10.1029/2011JC007006.
Rhines, P. B. (1979), Geostrophic turbulence, *Annu. Rev. Fluid Mech.*, *11*(1), 401–441.
Rio, M., and F. Hernandez (2004), A mean dynamic topography computed over the world ocean from altimetry, in situ measurements, and a geoid model, *J. Geophys. Res*, *109*, C12032, doi:10.1029/2003JC002226.
Risien, C., and D. Chelton (2008), A global climatology of surface wind and wind stress fields from eight years of QuikSCAT scatterometer data, *J. Phys. Oceanogr.*, *38*(11), 2379–2413, doi:10.1175/2008JPO3881.1.
Roquet, F., C. Wunsch, and G. Madec (2011), On the patterns of wind-power input to the ocean circulation, *J. Phys. Oceanogr.*, *41*(12), 2328–2342.
Schott, F. (1983), Monsoon response of the Somali Current and associated upwelling, *Prog. Oceanogr.*, *12*(3), 357–381, doi:10.1016/0079-6611(83)90014-9.
Schott, F., and J. McCreary (2001), The monsoon circulation of the Indian Ocean, *Prog. Oceanogr.*, *51*(1), 1–123, doi:10.1016/S0079-6611(01)00083-0.
Schott, F., and D. R. Quadfasel (1982), Variability of the Somali Current system during the onset of the southwest monsoon, 1979, *J. Phys. Oceanogr.*, *12*(12), 1343–1357.
Schott, F., J. C. Swallow, and M. Fieux (1990), The Somali Current at the equator: Annual cycle of currents and transports in the upper 1000 m and connection to neighbouring latitudes, *Deep Sea Res., Part A*, *37*(12), 1825–1848, doi:10.1016/0198-0149(90)90080-F.
Schott, F. A., S.-P. Xie, and J. P. McCreary (2009), Indian ocean circulation and climate variability, *Rev. Geophys.*, *47*(1), doi:10.1029/2007RG000245.
Shchepetkin, A., and J. McWilliams (2005), The regional oceanic modeling system (roms): A split-explicit, free-surface, topography-following-coordinate oceanic model, *Ocean Modell.*, *9*(4), 347–404, doi:10.1016/j.ocemod.2004.08.002.
Shetye, S., A. Gouveia, and S. Shenoi (1994), Circulation and water masses of the Arabian Sea, *J. Earth Syst. Sci.*, *103*(2), 107–123, doi:10.1007/BF02839532.
Shi, W., J. M. Morrison, E. Böhm, and V. Manghnani (2000), The Oman upwelling zone during 1993, 1994 and 1995, *Deep Sea Res., Part II*, *47*(7), 1227–1247, doi:10.1016/S0967-0645(99)00142-3.

© 2014. American Geophysical Union. All Rights Reserved.

Smith, K. S. (2007), The geography of linear baroclinic instability in Earth's oceans, *J. Mar. Res.*, *65*(5), 655–683, doi:10.1357/002224007783649484.

Smith, W., and D. Sandwell (1997), Global sea floor topography from satellite altimetry and ship depth soundings, *Science*, *277*(5334), 1956–1962, doi:10.1126/science.277.5334.1956.

Stark, J. D., C. J. Donlon, M. J. Martin, and M. E. McCulloch (2007), OSTIA: An operational, high resolution, real time, global sea surface temperature analysis system, in *OCEANS 2007-Europe*, pp. 1–4, Proceedings of Oceans '07 IEEE Conference, 'Marine Challenges: Coastline to Deep Sea', 18–21 June, Aberdeen, U. K.

Subrahmanyam, B., I. Robinson, J. Blundell, and P. Challenor (2001), Indian Ocean Rossby waves observed in TOPEX/POSEIDON altimeter data and in model simulations, *Int. J. Remote Sens.*, *22*(1), 141–167, doi:10.1080/014311601750038893.

Tulloch, R., J. Marshall, C. Hill, and K. S. Smith (2011), Scales, growth rates, and spectral fluxes of baroclinic instability in the ocean, *J. Phys. Oceanogr.*, *41*(6), 1057–1076.

Vallis, G. K. (2006), *Atmospheric and Oceanic Fluid Dynamics: Fundamentals and Large-Scale Circulation*, Cambridge Univ. Press, Cambridge, U. K.

Vecchi, G., S. Xie, and A. Fischer (2004), Ocean-atmosphere covariability in the western Arabian Sea, *J. Clim.*, *17*(6), 1213–1224.

Wiin-Nielsen, A. (1962), On transformation of kinetic energy between the vertical shear flow and the vertical mean flow in the atmosphere, *Mon. Weather Rev*, *90*(8), 311–323.

Wirth, A., J. Willebrand, and F. Schott (2002), Variability of the Great Whirl from observations and models, *Deep Sea Res., Part II*, *49*(7), 1279–1295, doi:10.1016/S0967-0645(01)00165-5.

Worley, S., S. Woodruff, R. Reynolds, S. Lubker, and N. Lott (2005), ICOADS release 2.1 data and products, *Int. J. Climatol.*, *25*(7), 823–842, doi:10.1002/joc.1166.

© 2014. American Geophysical Union. All Rights Reserved.